BIO-INSPIRED ADAPTIVE WINGTIP DEVICES FOR LOW REYNOLDS NUMBER
OPERATION

BY

MICHAEL K. LYNCH

THESIS

Submitted in partial fulfillment of the requirements
for the degree of Master of Science in Mechanical Engineering
in the Graduate College of the
University of Illinois at Urbana-Champaign, 2017

Urbana, Illinois

Adviser:

Assistant Professor Aimy Wissa

Abstract

Birds are highly capable and maneuverable fliers, traits not currently shared with current unmanned aerial vehicles. They are able to achieve these flight capabilities by adapting the shape of their wings during flight in a variety of complex manners. One feature of bird wings, the primary feathers, separate to form wingtip gaps at the distal end of the wing. This research presents bio-inspired wingtip devices with varying wingtip gap sizes, defined as the chordwise distance between wingtip devices, for operation in low Reynolds number conditions of Re = 100,000, similar to conditions experienced by many species of birds. Lift and drag data was measured for planar and nonplanar wingtip devices with the total wingtip gap size ranging from 0% to 40%. For a planar wing with a gap size of 20%, the mean coefficient of lift in the pre-stall region is increased by 7.25%, and the maximum coefficient of lift is increased by 5.6% compared to a configuration with no gaps. The nonplanar wingtip device was shown to reduce the induced drag. The effect of wingtip gap sizes is shown to be independent of the planarity/nonplanarity of the wingtip device, thereby allowing designers to decouple the wingtip parameters to tune the desired lift and drag produced. A light weight morphing mechanism design process is proposed, thereby enabling designers to build an adaptive wing that takes advantage of high lift benefits of having 20% wingtip gaps, useful for high payload conditions, as well as low drag benefits of having no gaps, useful for cruise conditions.

Acknowledgments

I would like to first and foremost thank Prof. Aimy Wissa for her continuous patience, guidance, resources, and general helpfulness. Without her to guide me, none of the work done over the last two years would be possible. She continually pushes me to achieve and dream big, and for that, I cannot thank her enough.

I want to also thank my lab mate and colleague, Boris Mandadzhiev. Boris has been an essential part of much of my work, allowing me to bounce ideas off of him and helping to keep me within the realm of reality.

The Renewable Energy & Turbulent Environment Group deserves many thanks for patiently lending the use of their facilities and assistance with wind tunnel tests.

Last but not least, I would like to thank the Mechanical Science and Engineering Department at the University of Illinois Urbana-Champaign for their continued support and resources throughout my graduate school experience.

Table of Contents

Nomenclature

α_b Base Wing Angle of Attack

α_t Wingtip Angle of Attack

δ SMA Coil Actuator Displacement

ϵ SMA Coil Actuator Extensional Strain

η SMA Coil Actuator Packing Density

γ Total Wingtip Gap Size %

ρ_∞ Air Density

θ Beam Angle

AR Aspect Ratio

b Total Wingspan

b_b Base Wing Span

b_t Wingtip Span

C Spring Index

c_b Base Wing Chord

C_{Di} Induced Drag Coefficient

C_{Dpr} Profile Drag Coefficient

C_D Drag Coefficient

C_{Lmax} Maximum Lift Coefficient

C_L Lift Coefficient

c_t Wingtip Chord

d SMA Wire Diameter

e Oswald's Efficiency Factor

e_{wl} Oswald's Efficiency Factor for Winglets

F_s	SMA Coil Actuator Force
G	SMA Shear Modulus (Martensite or Austenite)
h	Winglet Height
k_{wl}	Winglet Induced Drag Penalty Factor
l	Beam Length
L_0	SMA Coil Actuator Free Length (Martensite Phase)
Re	Reynolds Number
S	Wing Planform Area
t	Beam Thickness
u	Beam Translation
V_∞	Freestream Velocity

1   Introduction

Birds are highly capable and maneuverable fliers, with the ability to fly at both high and low speeds in a variety of flight conditions. They engage in a multitude of complex flight maneuvers, such as takeoff, landing, gliding, perching, diving, and more. Mission adaptability is enabled through changing the shape of their wings and their wing-beat gaits during flight in a variety of complex ways [1]. These abilities are not shared with today's small unmanned aerial vehicles (UAVs) [2].

Unlike birds, current small UAVs struggle to fly in gusty and turbulent conditions and are mostly relegated to fair weather flight [2]. Mohamed et al. assessed a variety of factors that prevent small UAVs from having stable flight characteristics including: low mass, power limitations, slow and low flight, and low Reynolds number conditions.

Among the factors affecting UAV flight, the low Reynolds number operating condition is perhaps the most significant obstacle to overcome. Airfoil performance diminishes at lower Reynolds numbers, decreasing the coefficient of lift and increasing the coefficient of drag [3]. In examining the efficiency of airplane airfoils in comparison with bird wings, Withers [4] demonstrates that bird wings perform similarly to conventional airfoils at low Reynolds numbers. Despite this, birds are still able to out maneuver and out perform UAVs. This demonstrates the need for a shift in approach away from optimizing airfoil shapes for low Reynolds numbers, and instead, looking to birds for inspiration on adaptive wing structures.

When examining birds' wings, there are many notable feather systems used by birds to improve mission adaptability. These include the primaries, the secondaries, the coverts, and the alula feathers [5]. Each category of feather has a different function relating to flight. In particular, the gaps between primary feathers have been shown to reduce the induced drag [6]. Inspiration from birds' wingtips can provide insight on how to improve the wingtip design of small UAVs. However, for a small UAV to achieve the performance capabilities demonstrated in birds, an adaptive wingtip device that alters wingtip geometry, similarly to how birds are able to alter their wing geometry, is required.

The objective of this research is to quantify the effect of wing gaps, as seen in Figure 1, at low Reynolds number conditions on the lift and drag of a wing over an angle of attack sweep of the pre-stall and stall regions. The effect of Reynolds number, wingtip angle of attack, and wingtip planarity (as seen in Figure 2) at different gap sizes will be investigated. The goal will then be to give design recommendations for an efficient wingtip device system that produces high lift, while minimizing drag (focusing on induced drag), at low Reynolds numbers. The second portion of this research will focus on the design of a morphing mechanism for the deployable wingtip devices, as characterized in the first
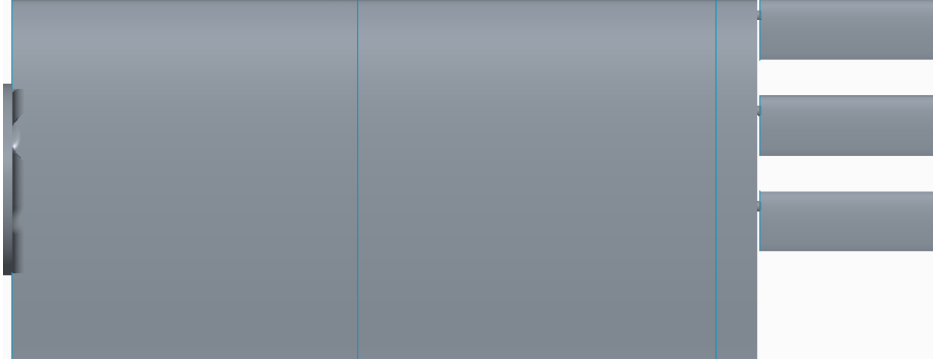
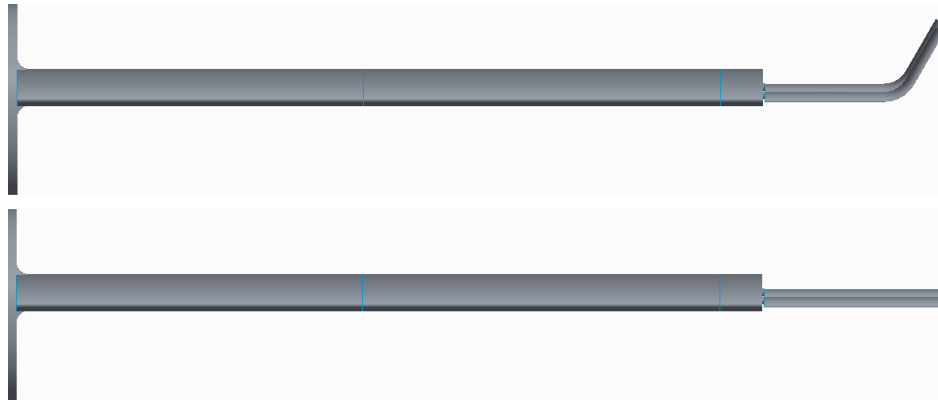Figure 1: Top view of experimental setup with $\gamma = 20\%$.

Figure 2: Top: Nonplanar wingtip configuration. Bottom: Planar wingtip configuration.

portion of the research. These morphing mechanism will allow UAVs employing wingtip gaps to adapt to varying environmental conditions, increasing the mission capabilities of those UAVs by improving the factors such as range and payload capabilities.
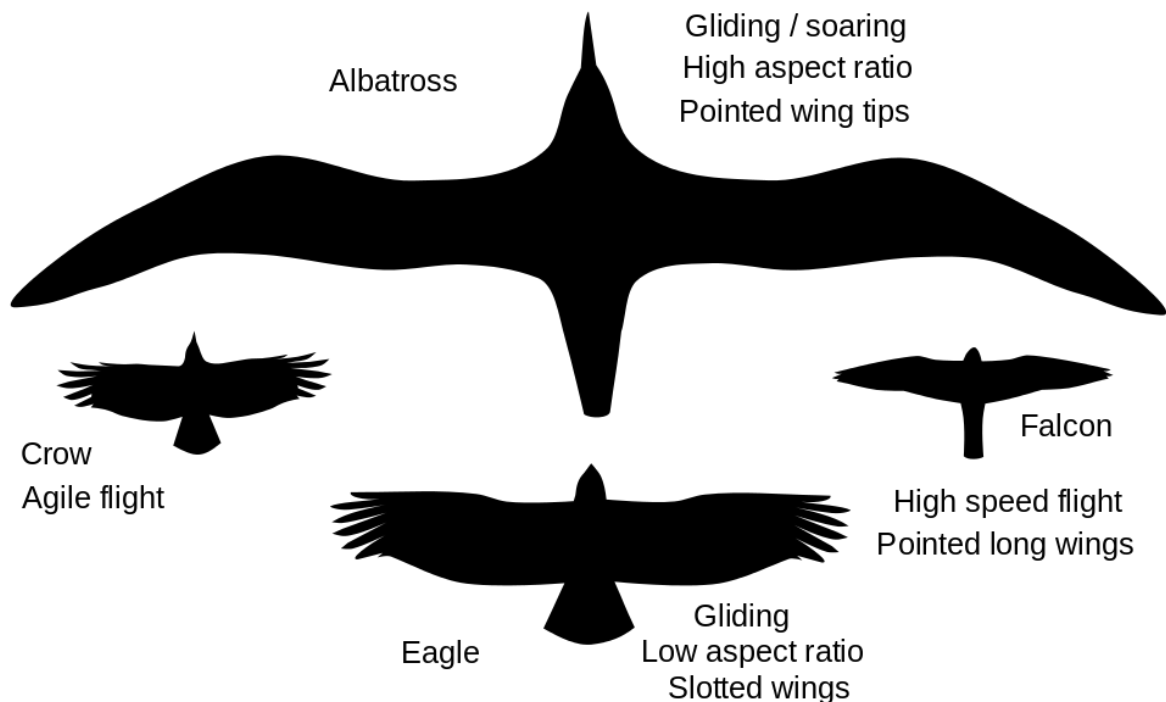
Figure 3: Wing Shapes: Soaring Wings, High Speed Wings, High Lift Wings, and Elliptical Wings. Bird flight silhouettes By L. Shyamal (Own work) [CC BY-SA 2.5 (`http://creativecommons.org/licenses/by-sa/2.5`)], via Wikimedia Commons.

2 Literature Review

2.1 Background on Avian Wingtip Devices

Birds provide a natural inspiration for flight, able to move effortlessly through the air while performing complex maneuvers in adverse flight conditions. Their wings continuously morph, allowing birds to adapt to new flight conditions. To begin to understand how birds are able to do this, their wings must be analyzed in greater detail.

When categorizing bird wing planforms, there are generally four different types as seen in Figure 3: soaring wings, high speed wings, elliptical wings, and high lift wings [7].

Small UAVs fly in environments that are relatively close to ground level, filled with obstacles such as trees and buildings, and characterized by high levels of turbulence [8]. Among the previously mentioned categories, two types of bird wing shapes operate in similar conditions: elliptical wings and high lift wings. Elliptical wings, as seen on birds such as crows, have a shape approaching that of an ellipse, allowing for high degrees of maneuverability [7]. High lift wings, as seen on eagles and hawks, are used by birds of prey that need to carry

3

Figure 4: Wingtip gaps of a bald eagle.

large payloads. Wings of high lift birds have greater agility than soaring wings or high speed wings. In particular, high lift wings have similar requirements as wings used by modern UAVs due to the payload demands of UAVs, and as such, they will be the focus of this study.

When looking at various wing structures present on high lift wings, one notable feature is the presence of wingtip gaps as shown in Figure 4. These gaps are created as a result of separation of primary wingtip feathers, due to primary feather emargination. Some bird feathers are not shaped like ellipses, but instead have a tapered region, and the emargination of the bird feathers is the point at which the taper begins. As can be seen in Figure 5, the emargination is where the feather tapers at the leading edge, and the notch is where the feather tapers at the trailing edge. While it varies for different species, usually the first 5 - 6 feathers have significant emargination, as seen in Figure 6. This is because these are the feathers that form the leading edge of the wing while the remaining feathers form the trailing edge.

To understand the effect wing gaps, created from the emargination and notch on avian feathers, have on bird flight characteristics, Tucker conducted wind tunnel experiments on a Harris Hawk wing [6]. Tucker found that wing gaps reduced the induced drag, the component of drag generated due to the lifting force, of a Harris Hawk wing by acting as nonplanar winglets and spreading the vorticity both horizontally and vertically. The reduction of

4

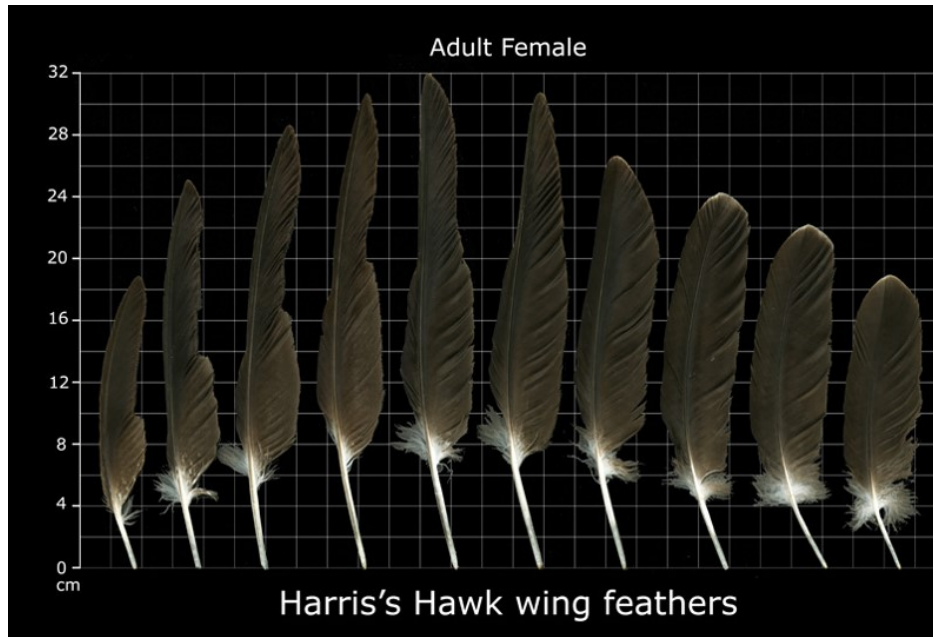Figure 5: Bird Feather Emargination. Credit: *U. S. Fish and Wildlife Service* `https`: `//www.fws.gov/lab/featheratlas/`

Figure 6: Primary feathers of an adult Harris Hawk. Credit: *U. S. Fish and Wildlife Service*
`https://www.fws.gov/lab/featheratlas/`

induced drag is especially important for birds because, at low Reynolds number, the primary
flight regime of most birds, the induced drag is the dominant component of drag. These low
Reynolds number effects are also important to the design of small UAVs which operate at
similar Reynolds numbers to birds and are also impacted by induced drag being a large
component of the total drag [9].

2.2   Background on Engineered Wingtip Devices

The work done by Tucker [6] shows that nonplanar winglets play an important role in
reducing the induced drag of avian flight. These ideas are not new, and research has been
conducted on various wingtip devices for decades. Studies of nonplanar structures, such
as winglets, were first rigorously conducted by Whitcomb. Whitcomb [10] showed that
the induced drag on airplanes can be reduced by 20% under certain conditions with the
incorporation of properly designed winglets. This is a significant benefit since induced drag
can make up 40% of an airplane's drag under cruise conditions and up to 80 - 90% of drag
under takeoff conditions [11].

McLean summarizes and explains in great detail the underlying physics behind how
winglets work and how the various components of drag are affected by the introduction of
winglets [12]. McLean discusses the important factors in winglet design, citing benefits such
as reduced induced drag, improved range, reduced noise, and more while also discussing

some of the offsetting factors such as increased weight, increased structural requirements, increased cost and developmental risk. McLean also presents some case studies of winglet designs, especially in the case of the API winglet on the 737NG.

In the 2001 Annual Review on fluid Mechanics, Kroo provided an extensive overview on concepts and considerations behind induced drag prediction and reduction, going beyond wingtip devices and consider an entire flight system [9]. Details are given on several approaches, undertaken by various researchers to reduce induced drag, with inconclusive results. Depending on what factor is held constant, including span, root bending moment, wing area, etc., different approaches provide valid results for reducing induced drag. Kroo shows that induced drag cannot be reduced significantly without affecting lift, and instead, reductions in induced drag are likely to be small, incremental improvements in the future, especially in the context of high aspect ratio subsonic wings.

Despite all of this research and development, according to the author's knowledge, there have been very few and limited instances of research conducted on winglets for low Reynolds number conditions where small UAVs usually perform. Much work done on wingtip devices, such as the work done by La Roche [13] and Fluck [14], have all focused on larger vehicles which operate at higher Reynolds numbers ($Re \geq 10^6$).

La Roche and Palffy classified methods of reducing induced drag through wing design into four different categories: contour (swept wings), endplate, open fan-like (Whitcomb winglet), and closed multiple [13]. La Roche and Palffy's wingtip device, the WING-GRID, falls into the fourth category that seeks to reduce induced drag by increasing the vortex spacing and increasing the vortex radius of the shed vortices. The results of the WING-GRID design showed promise with claims of a reduction in induced drag of up to 50%. However, the benefits of such a device are debated and instead, Kroo believes that the local coefficient of lift is improved with limited induced drag benefits [9].

Fluck and Crawford's work focused on a lifting line approach to modeling bio-inspired wingtip geometries at $Re = 1.3 \times 10^6$ [14]. They ran a parametric study of over 100 different configurations, assessing factors such as number of winglets which represented bird feathers, winglet dihedral, winglet twist, and winglet sweep on the glide ratio and wing performance polar (C_L vs C_D). The authors found that the optimal winglet device geometry was very application specific and did not identify a configuration that maximized both lift as well as the glide ratio. They also found that their wingtip devices were very sensitive to winglet twist and that the individual winglets needed to have different twist values to gain see any benefit in the glide ratio.

Among the work that considers low Reynolds operation, the most relevant are the works done by Muñoz and Catalon [15], Guerrero et al. [16], and Smith et al. [17]. Muñoz and

Catalon's work examined the effect of tip sails, small wing-like plates attached at various dihedral angles to the end of a wing, at $Re = 3.5 \times 10^5$. Their results showed that the inclusion of tip sails outperformed a clean wing in terms of C_L/C_D, climb factor, and range factor. The results gave insight into which configurations perform well in a variety of flight regimes, though more work would need to be done to find optimal configurations.

Guerrero et al. used a computational fluid dynamics approach to understanding how spiroid wingtips functioned at $Re = 1.0 \times 10^5$ [16]. Guerrero et al. found that in the pre-stall region, there was a 9.0% improvement in C_L for the spiroid wingtip as opposed to a clean wing. The authors also found that the spiroid wingtip was able to delay stall, and once stall occurred, C_L tapered off more gradually for the spiroid as compared with a clean wing. When examining the drag polar, they determined that the spiroid wingtip was only more efficient than the clean wing for a given C_L when at angles of attack above 3.5°.

Smith et al. examined the lift to drag ratio on a multi-winglet configuration in low Reynolds number conditions ranging from 1.61×10^5 to 3.0×10^5 and concluded that the ratio was improved by 15 - 30% for a configuration where the winglet dihedral angle is varied as compared with a configuration angle with constant dihedral angle [17]. However, despite this overall improvement in the lift to drag ratio, while the actual lift force increased, the overall drag force also increased.

Many questions remain about how exactly wingtip devices affect induced drag, especially at low Reynolds numbers. The goal of the aerodynamic testing conducted in this study is to develop a more complete understanding of how wingtip gaps and planarity affect the aerodynamic performance of a wing designed for a small UAV at low Reynolds numbers. Specifically, this research seeks to understand what if any use case there might be for deployable wingtip gaps and if the wingtip devices should have a nonplanar or even flexible element to them.
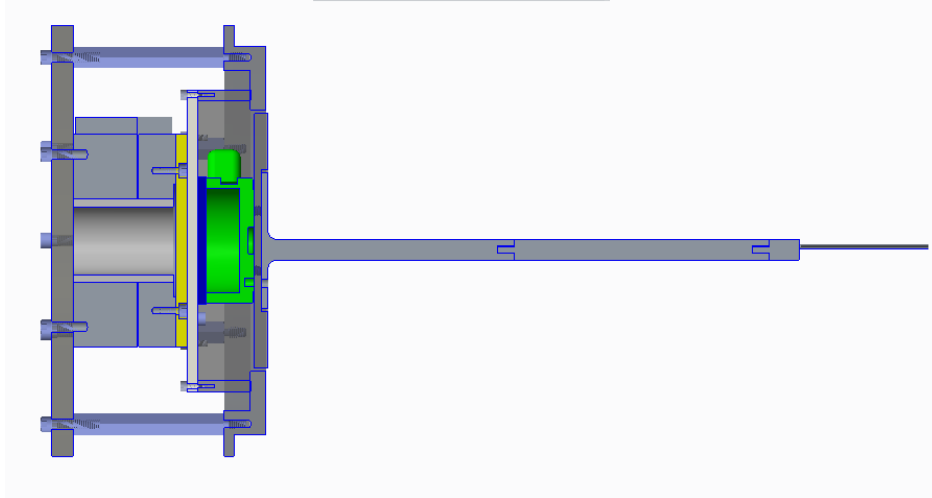
Figure 7: Experimental setup showing the custom housing with Velmex rotary table and ATI Gamma force/torque transducer.

3 Methods

3.1 Aerodynamic Experiment

3.1.1 Experimental Setup

For the aerodynamic portion of this study, extensive wind tunnel testing was conducted. Tests were conducted in an open-loop, constant pressure wind tunnel with a cross section of 90 cm by 45 cm at the University of Illinois Urbana-Champaign. The wind tunnel has four equal length sections, and the first section was chosen for testing due to having the smallest boundary layer thickness and least turbulence.

The tested wing system, which consists of the base wing and the wingtip devices, was mounted to a custom-made housing system in the sidewall of the wind tunnel as shown in Figure 7. The housing system contained a Velmex B48 rotary table which was used for precision control of the base wing angle of attack, α_b. A micro stepper driver was used to control the stepper motor that turned the Velmex rotary table. The micro stepper driver was set to take 2 micro steps per motor step so as to increase the resolution of the stepper driver while still outputting enough torque to turn the rotary table. Using a 200 step/revolution stepper motor, 2 micro steps/motor step, and a 72:1 gear ratio in the rotary table, the rotary table could be accurately controlled to within 0.0125°, which was more than sufficient for controlling α_b. The rotary table was controlled using an arduino script via a command line interface. The system required either an input of the number of degrees to rotate, or the number of micro steps to move in a specified direction. The wiring diagram for the arduino,
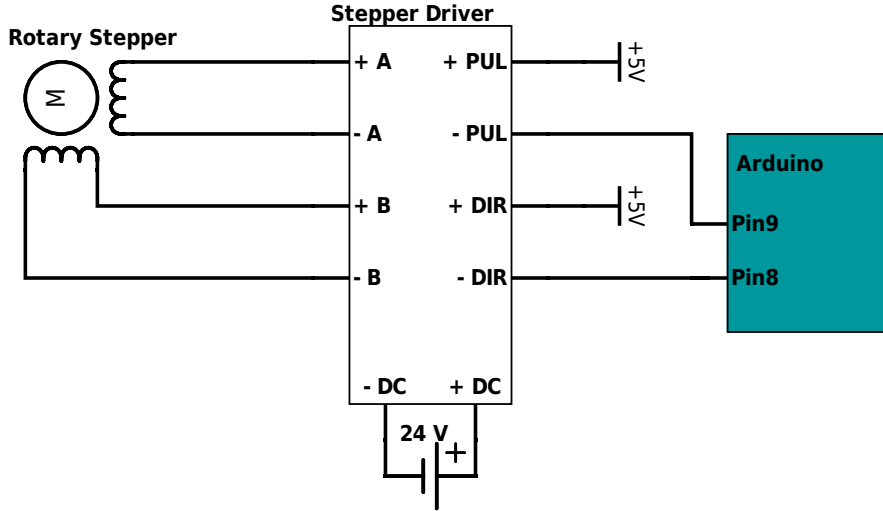
9

Figure 8: Velmex Rotary Table Wiring Diagram

stepper motor driver, and stepper motor is shown in Figure 8.

Attached to the rotary table and within the custom housing was an ATI Gamma 6-axis force/torque transducer, used to collect the lift and drag forces on the wing. The ATI Gamma load cell was calibrated to the SI-32-2.5 specifications by ATI. In the lift and drag directions (the sensor X and Y axes), the force/torque transducer had a range of up to 32 N and a resolution of 1/160 N for force and a range of 2.5 Nm and 1/2000 Nm for torque. These ranges were important to keep in mind when sizing the wing system so as to avoid saturating the transducer. The resolution of the transducer was sufficient for accurately measuring the lift and drag forces on the wing system.

The wind tunnel flow velocity was controlled by adjusting the fan frequency. To determine the flow velocity at the given test section, a static-pitot tube attached to a differential pressure sensor was placed near the desired test location when the wind tunnel was empty. The wind tunnel was set to a variety of fan frequencies and sensor pressure values were recorded. By accounting for temperature, pressure, and humidity conditions, the flow velocity could be determined from the pressure values. Using the base wing chord length, c_b, as the characteristic length for the Reynolds number, a relationship between fan frequency and Reynolds number could be determined. The relationship was found to be highly linear across the entire range of tested fan frequencies. The wing system was then tested at three different Reynolds numbers, $Re = 7.5 \times 10^4$, $Re = 1.0 \times 10^5$, and $Re = 1.5 \times 10^5$. Due to the cross sectional size of the wind tunnel being significantly larger than the size of the wing system, blockage effects were considered negligible and not accounted for.
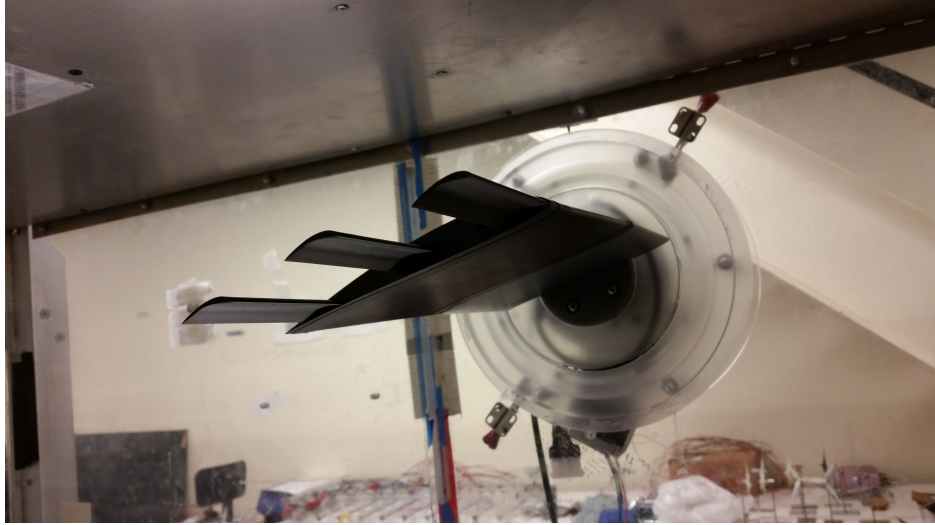
Figure 9: Experimental setup with $\gamma = 40\%$ and the $(0, 0, 0)$ configuration for α_t.

3.1.2 Wing and Wingtip Parameters

In this experiment, the wing and wingtip device geometry were modeled after the Harris Hawk. The base wing is a rectangular wing with an SD7032 airfoil profile, designed to operate in low Reynolds number conditions. The base wing chord length, c_b, is 150 mm and the wing has a semi-span, $b_b/2$ of 312.5 mm.

Measurements were taken of a Harris Hawk's primary feathers from digital images obtained from the Feather Atlas [26]. These were used as a basis for the geometry of the wingtip devices, modeled in this experiment as wings S1091 airfoils as the profile. Based on the geometry of the Harris Hawk primary feathers, the chord length of one wingtip, c_t, was found to be 16.7% of the c_b, or 25 mm and the wingtip span, b_t, was found to be 12% of the base wingspan, b_b, or 75 mm.

A nonplanar wingtip was designed such that b_t and c_t were the same as for the planar wingtips. The nonplanar wingtip height, h, was set at 7.5% of the semi-span of the wing-winglet system as described in Equation 1. The wingtip cant angle was set to 60°, and the winglet bend radius was set to 50% of h.

$$h = \left(\frac{b_b}{2} + b_t \right) 0.075 \tag{1}$$

A planar configuration is defined as the base wing with three planar wingtips, while a nonplanar configuration is defined as the base wing with three nonplanar wingtips. In addition to the planar and nonplanar configurations, a baseline wingtip extension was tested. The baseline test was designed such that the base wingspan was increased to maintain the

11

overall span of the wing-wingtip system.

The overall aspect ratio of the wing and wingtips was 5.72, which falls in the range of 4 - 6 for the AR of high lift wings [7]. The wingtip extension had an aspect ratio of 5.17 since the wingtip extension had the same span, but a larger planform area, S.

The total wingtip gap size percentage, γ, is defined as total gap spacing between all of the feathers/wingtip devices divided by the base wing chord length. From images of a Harris Hawk with its wings fully spread, the gap size between each feather, measured at the feather tips, is measured to fall in the range of 12 - 22% of the mean chord of the wing, c_b, averaging 17%. Comparing that to a wing with 3 feathers, as shown in Figure 10, the equivalent γ of a Harris Hawk would be 35%. The γ value for the Harris Hawk is artificially high due to the taper of the feathers, leading to uneven gap sizes. An alternative measurement might be to measure the average gap size over the wingtip gap region, however, the wingtip gap region is not well defined varying between individual specimen. As such, the γ value of the Harris Hawk at the wingtip was used.

3.1.3   Test Configurations

Several wing-wingtip system configurations were tested. The planar and nonplanar wingtips were tested with varying gap sizes, γ, of 0%, 20%, 30%, and 40%. Gap sizes $\gamma = 0\%$ and $\gamma = 40\%$ are shown in Figure 10. For each configuration, the base wing angle of attack, α_b was varied from 6° to 21° except when $Re = 7.5 \times 10^4$. At this Reynolds number, stall occurred much earlier and testing was limited from 6° to 15°. Testing at these angles of attack allowed for detailed measurements of aerodynamic forces in the pre-stall and post-stall regions.

In flight, the wingtips of birds are offset at various angles of attack due to the interaction with the air. Graham explains that the wingtips twist forward, bend upward, and bend forward as a result of the wingtips yielding to the reaction of the displaced air. The wingtips, offset at various angles of attack, deflects the air such that the direction of the air stream is gradually changed [27]. To account for the effect of the wingtip angles of attack, the wingtips were set at an angle of attack relative to the base wing in 4 different configurations as shown in Table 1. The shaft attaching the wingtips to the base wing were located at the $c_t/4$ location. The hole locations for the wingtip shafts were located along the camber line of the base wing.

Figure 10: Top: Wing-Wingtip configuration with $\gamma = 0\%$. Bottom: Wing-Wingtip configuration with $\gamma = 40\%$.

Table 1: Sets of tested wingtip angles of attack, α_t

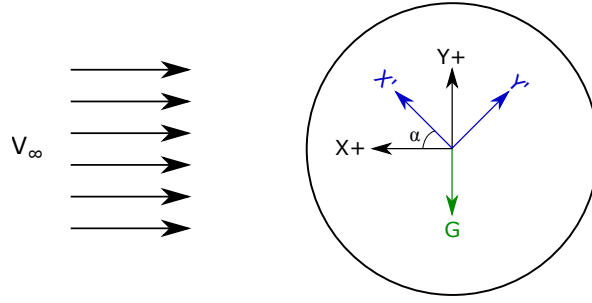| Leading α_t	Secondary α_t	Trailing α_t
0°	0°	0°
-10°	-5°	0°
-10°	0°	10°
-10°	-10°	-10°

Figure 11: Force/Torque transducer axes with respect to free stream velocity

3.1.4 Data Logging and Processing

The force/torque data from the ATI Gamma force/torque transducer was acquired using an NI USB 6210. A Windows executable, supplied by ATI, was used to record the values from the NI data acquisition device. The sample rate for each test was set at 1 kHz, and each test was logged for 10 seconds while in steady state. The logged data was then averaged to obtain the force and torque values for a given test run. Because the force/torque transducer rotated with the base wing, and because the it was zeroed only at the zero angle of attack position, a rotation matrix that accounted for mass offloading one axis and loading another was used. Figure 11 shows the force/torque transducer axes used.

To compensate for the mass effect, the mass of both the wing system as well as the internal mass of the force/torque transducer must be known. If there was no wing system and the force/torque transducer was rotated, there would still be a mass loading effect, and this mass is referred to as the transducer internal mass. The mass of the wing system and transducer internal mass were obtained experimentally. The transducer is first set to $\alpha = 0°$ and zeroed. Rotating the transducer 90° will completely offload one axis and load the other. The 2-norm of the F_X and F_Y force values can be taken to be the total weight, W, of the system.

After determining the weight of the system, the weight must be compensated for before applying the rotation matrix so as to recover the lift and drag data. Figure 11 shows how W affects each of the transducer axes. When the transducer is set at some angle of attack, α, the gravitational force is $W \sin(\theta)$ in the negative X' direction and $W \cos(\theta)$ in the negative Y' direction. To recover the lift and drag forces, the gravity effects are added to the F_X and F_Y forces since the gravitational force acts in the negative direction on both axes.

Since the transducer is zeroed at $\alpha = 0°$, the force on the Y axis is 0, which is W larger than it should be. This relationship holds true for all other α. To account for this effect, W

must be subtracted from the F_Y force. This biasing effect does not affect the X axis since it is unloaded when the transducer is zeroed.

The final step is to flip the direction of the mass compensated F_X force so as to align it with the drag direction. Combining all of these steps together yields Equation 2.

$$\begin{bmatrix} L \\ D \end{bmatrix} = \begin{bmatrix} \cos(\alpha) & -\sin(\alpha) \\ \sin(\alpha) & \cos(\alpha) \end{bmatrix} \begin{bmatrix} F_Y - W(1 - \cos(\alpha)) \\ -F_X - W\sin(\alpha) \end{bmatrix} \tag{2}$$

3.2   Morphing Mechanism

3.2.1   Overview of Bistable Structures and Shape Memory Alloy Actuators

Along with understanding the underlying aerodynamics of wingtip gaps, it is essential to be able to morph the wings and deploy the wingtip gaps in response to environmental conditions. Morphing wings can be achieved with either a passively tuned response to environmental conditions, or with active control to compensate for environmental conditions. In this research, wingtip gap morphing is achieved by using an actively controlled shape memory alloy actuator attached to a bistable structure, forming the morphing mechanism.

In the analysis of beams under compression, beams have been shown to deform under a critical load at which point they assume an equilibrium configuration distinctly different from the configuration immediately prior to reaching the critical load; this is referred to as buckling. Buckling in beams can take many forms including classical buckling, finite-disturbance buckling, and snapthrough buckling [18]. Among these forms of buckling, snapthrough buckling is of particular interest due to the existence of two distinct stable configurations, thereby forming a bistable structure. The properties of this bistable structure can be taken advantage of in designing a two-state actuator.

A model of a structure which undergoes snapthrough buckling as well as a typical load-deflection curve of such a structure is depicted in Figure 12. As can be seen in the load-deflection curve, when the load increases beyond a certain point, the structure undergoes a very large displacement. This is a result of the structure becoming unstable and transitioning from one previously stable configuration to a new stable configuration. Therefore, by using a bistable structure, an actuator can apply a small incremental force that produces a large stroke. This enables the use of a different class of actuators that would have otherwise been impractical to use.

In the application of a bistable structure for the wingtip gaps, the use of such a structure is important because it allows the wingtip gaps to be set at two different states: undeployed and deployed. The aerodynamic performance of wingtip gaps changes when in one state or the other, and the differences between these states can be exploited to create adaptive
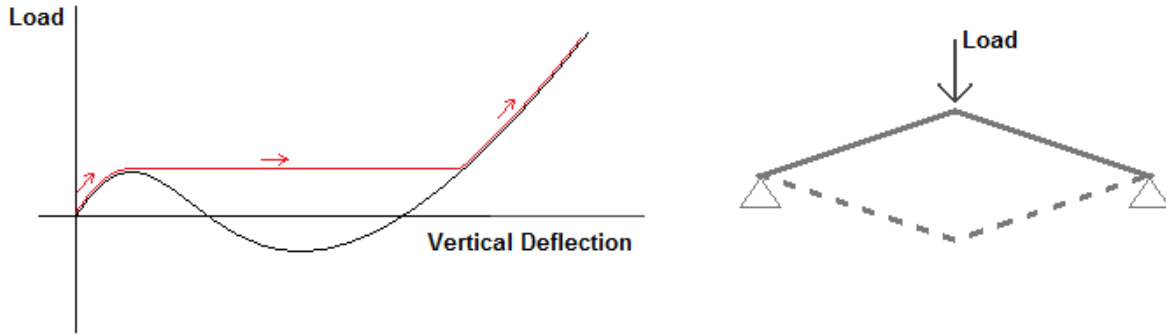
Figure 12: Left: Force deflection curve for a bistable structure which undergoes snapthrough buckling. Right: Model of snapthrough buckling structure.

wingtip devices. The bistability is important because it allows for lower power requirements, only requiring energy to move the system from one state to the other and not requiring a continuous energy input to maintain a state. A linearly translating bistable structure has already been designed and analyzed by Shan et al. [19] and can be adapted to work in an aerodynamic setting.

To actuate the bistable structure, a light weight, low power, large stroke linear actuator must be used. There are few devices that fit these requirements, but one possible device is the artificial muscle, nylon fishing line based actuator designed by Haines et al. [20]. The artificial muscle contracts when heated and expands when cooled, producing 5.3 kW/kg of actuator weight. Mirvakili et al. demonstrated a way of coating the artificial muscle with a silver paint to allow for an electrically controlled actuation method via joule heating [21]. However, despite claims of a stroke of up to 49%, it is difficult to create actuators that maintain strength while having a stroke much larger than 5 - 10%.

An alternative actuator that can be used is a Nickel-Titanium (NiTi) shape memory alloy (SMA). Heating up the NiTi SMA results in a 2 - 3% length contraction as the phase changes from martensite to austenite. For many applications, while the load bearing capacity of the NiTi SMAs is significant, the stroke is too small to be of use. However, by coiling the NiTi wire, many researchers have been able to make NiTi coil actuators. These NiTi coil actuators are often modeled using a simple mechanical spring model using different shear moduli, one for the austenitic phase and one for the martensitic phase [22].

Holschuh and Newman demonstrated the use of this simple model in the context of low spring index SMA coil actuators [23]. They designed their SMA coil actuator to maximize output force for a given SMA wire diameter as well as other physical constraints. Their

resulting actuator exhibited a highly linear force-displacement relationship even at strains of up to 300%.

Kim et al. and Seok et al. expand on the basic mechanical spring model for their "Meshworm" robot [22, 24]. Their model takes into account the change in the free length of the NiTi coil actuator due to phase change as well as accounting for the NiTi coil diameter change as the coil is elongated in the martensite phase. Kim et al. and Seok et al. also provide a detailed process for consistently manufacturing NiTi coil actuators as well as providing force-deflection data for coil actuators that were annealed at different temperatures ranging from 300°C to 540°C.

An et al. created a two-state model that takes into accounts for nonlinear effects such as the nonlinear detwinning effect of the SMA and the nonlinear geometric effect of the coil spring for large deformations [25]. This model, while being more sophisticated than previous models, is still simple enough to be used in a preliminary design stage without resorting to using numerical computational tools used in thermomechanical models of SMA coil actuators. An et al. created a design process flow for specifying the geometry of the SMA coil actuators based on specified force and deflection parameters.

By combining the NiTi SMA coil actuator with the bistable structure developed by Shan et al., a morphing mechanism can be developed. The goal of the morphing mechanism portion of this research is to develop a design process for a low weight, large stroke actuator that can repeatably and reliably deploy wingtip devices, as described previously, and alter the wingtip gap size during flight conditions.

3.2.2 Bistable Structure Design

This section covers the design of a bistable structure for use in a morphing mechanism. The bistable structure is heavily based off of the design parameters from Shan et al. [19]. In the design of their multistable structure, the authors characterized their device using two parameters: θ and t/l as seen in Figure 13. These two parameters determine whether or not the structure is bistable, and if it is bistable, how much energy it can store.

The goal of this research is to develop a morphing mechanism that can deploy wingtip gaps from $\gamma = 0\%$ to $\gamma = 20\%$ for a wing with $c_b = 150\,\text{mm}$. Therefore, the beam, circled in blue in Figure 14, was designed to translate a distance of $u = 15\,\text{mm}$ and $u = 30\,\text{mm}$ for the middle wingtip device and the trailing wingtip device respectively. The beam angle, θ, was chosen to be 50° and the thickness to length ration, t/l, was chosen to be 0.1. These choices of parameters put the structure well into the bistable region as seen in Figure 13. To ensure that the beam could translate far enough to enter into the bistable configuration, u had to be larger than the vertical height of the beam, $l\sin(\theta)$. Multiple trials found that Equation
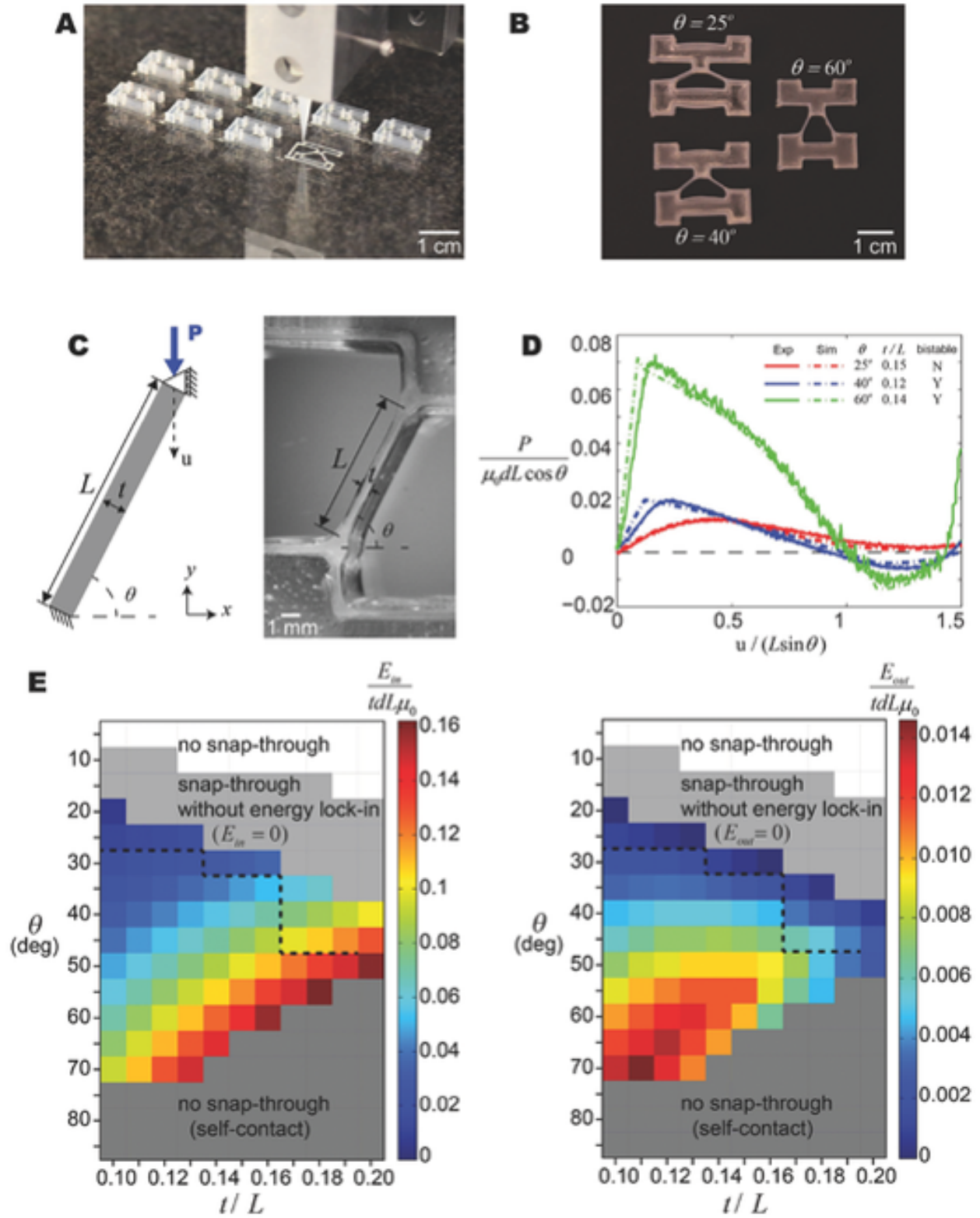
Figure 13: Reused with permission from [19]. Advanced Materials Volume 27, Issue 29, pages 4296-4301, 18 JUN 2015 DOI: 10.1002/adma.201501708 http://onlinelibrary.wiley.com/doi/10.1002/adma.201501708/full#adma201501708-fig-0002

3 is a sufficient condition relating u and l to reliably achieve bistability. With the choice of these parameters, the geometry of the bistable structure is fully defined.

$$u = 2l \sin(\theta) \tag{3}$$

Since the bistable structure is required to fit inside of a wing such as the SD7032 wing used in the aerodynamic portion of this research, the thickness of the structure is limited. The thickness of the structure does not affect the bistable nature, and instead, it is directly related to the amount of energy required to move the system from one stable configuration to the other. Due to the presence of aerodynamic forces acting on a wingtip device, the energy required to move the system from one configuration to the other should be maximized so that the device is actuated only by the internal actuator, and not the externally applied aerodynamic load. For this experiment, the thickness of the bistable structure was chosen to be 1 cm. This thickness is less than the thickness of the SD7032 base wing.

To make the bistable structure, a negative mold of the structure was 3D printed using an FDM printer with ABS as the material. The molds were prepared by first spraying them with EaseRelease and then filling them with a two part silicone material, Mold Max 10. After letting the structure cure for 24 hours, the silicone structures were removed from the mold. The CAD model of the mold as well as the final results are shown in Figure 14.

When mounted to the base wing, one end of the bistable structure would be fixed, and the other end as well as the middle portion of the structure would be able to move 15 mm each. The middle wingtip device would be attached to the middle of the bistable structure, and the trailing edge wingtip device would be attached to the moving end of the structure. The thicknesses of the middle portion and the trailing portion of the bistable structure would need to be adjusted to account for the chord of the wingtip devices, c_t. A low friction coating would need to be applied to the bistable structure to allow it to freely slide within the base wing. Doing this would allow the wingtip devices to actuate from the $\gamma = 0\%$ configuration to the $\gamma = 20\%$ configuration.

3.2.3 Shape Memory Alloy Design

The development of the Shape Memory Alloy (SMA) coil actuators follows the processed for low index coil actuators developed by Holschuh and Newman [23]. Low temperature Flexinol, a material similar to Nitinol, was purchased from Dynalloy to develop the SMA coil actuators.

Following the design parameters from Holschuh and Newman, the spring index, C, was chosen to be as low as possible without encountering physical limits of the minimum cur-
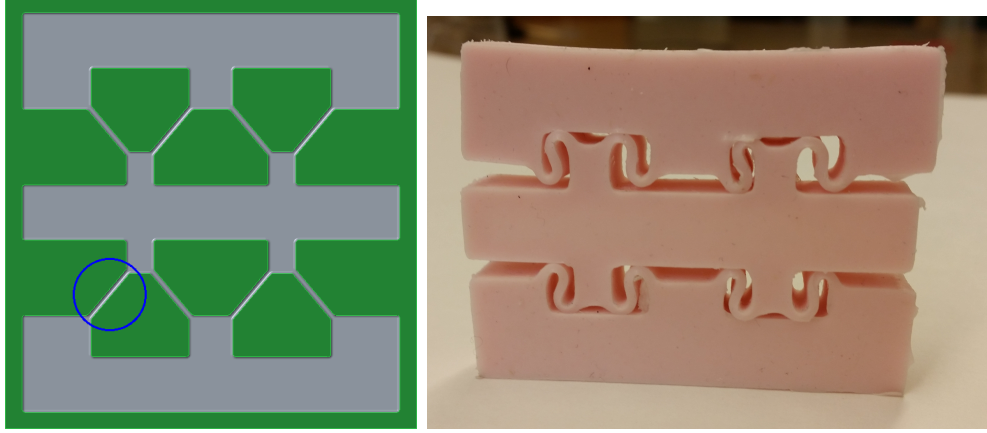
Figure 14: Left: Bistable structure mold for structure in extended configuration with beam circled in blue. Right: Bistable structure after removing from mold in compressed configuration.

vature of the spring. As such, the chosen value was $C = 3$. The diameter chosen for the Flexinol wire was $d = 200\,\mu\text{m}$, although Dynalloy sells a wide variety of different diameter Flexinol wires. The packing density, $\eta = 1$, was chosen to be as dense as possible for ease of manufacturing. In practice, it is hard to exactly achieve $\eta = 1$, and a conservative estimate of $\eta = 0.85$ is used instead. The final design parameter is ϵ, the extensional strain of the actuator as described in Equation 4.

$$\epsilon = \frac{\delta}{L_0} \tag{4}$$

To apply an SMA coil actuator to the bistable structure shown in Figure 14, the biggest constraint is space. The endpoints of the SMA coil actuator must be placed such that in the compressed configuration, the spring is equal in length to L_0 or longer. The displacement of the beam should be equal to the displacement of the spring, or in other words, $u = \delta$. By defining the attachment points of the SMA coil actuator as well as using the displacement constraint, ϵ can be determined.

The output force of the SMA coil actuator can then be calculated in accordance with Equation 5.

$$F_s = \frac{Gd^2}{8C^3\eta}\epsilon = \frac{Gd^2 u}{8C^3\eta L_0} \tag{5}$$

The force output of the SMA coil actuator can then be tuned by varying d, C, and L_0 for a given G, u, and η [23].

For a given bistable structure, a force vs displacement graph similar to Figure 13D should be experimentally obtained. F_s can then be compared against this force graph to ensure that
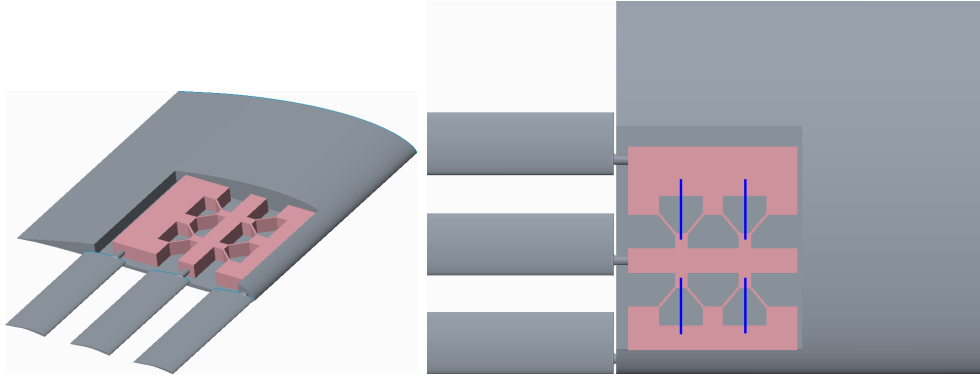
20

Figure 15: 3D view and top view of Morphing Mechanism in Sd7032 wing. The blue lines in the top view represent where the SMA coil actuators would be acting.

the SMA coil actuator can apply enough force to move the bistable structure from one stable configuration to the other. Considerations should also be taken for the drag force on the wingtip device which may or may not be negligible depending on wingtip geometry and operating conditions. The force-displacement curve of the bistable structure can be adjusted by changing the thickness of the structure as well as the shear modulus of the material used to create the bistable structure, all without affecting the bistability of the structure. The end result should be an SMA coil actuator capable of moving the bistable structure from one configuration to the other, all while under an aerodynamic load.

In application, two SMA coil actuators will be needed and used in an antagonistic fashion. Each SMA coil actuator will be able to contract when heated. There are many possible configurations of bistable structures and SMA coil actuators that will achieve the desired displacement. One possible configuration would be to have one end of a SMA coil actuator attached to a fixed connection point towards the trailing edge of the wing, and the other end attached to the free end of the bistable structure. This would deploy the wingtip from the $\gamma = 0\%$ configuration to the $\gamma = 20\%$ configuration. Likewise, to move from the $\gamma = 20\%$ configuration to the $\gamma = 0\%$ configuration, an SMA actuator would have one end attached to a fixed connection point near the leading edge of the wing and the other end connected to the free end of the bistable structure. In this configuration, $u = 30\,\mathrm{mm}$ for both coil actuators. For connection purposes, part of the SMA coil actuator can be left uncoiled as a straight wire, allowing the device to be used across larger distances. If this is done, then it is important to take into account the fact that the straight wire will contract by 2 - 3%, which depending on the length of the straight portion, may or may not be significant relative to the SMA coil actuator contraction, δ.

4 Results and Discussion

The following results presented are select results showcasing the main effects observed from the experiments conducted.

4.1 Effect of Reynolds Number

For the aerodynamic tests conducted, the non-dimensional lift and drag coefficient were calculated from the force transducer data and based on the geometric and test parameters in accordance with Equations 6 and 7. These values were used to create C_L vs α_b graphs as well as C_L vs C_D graphs, thereby characterizing the aerodynamic performance of each configuration under the specified testing conditions.

$$C_L = \frac{L}{\frac{1}{2}\rho_\infty V_\infty^2 S} \tag{6}$$

$$C_D = \frac{D}{\frac{1}{2}\rho_\infty V_\infty^2 S} \tag{7}$$

Tests for the planar configuration were conducted at three different Reynolds numbers: $Re = 7.5 \times 10^4$, $Re = 1.0 \times 10^5$, and $Re = 1.5 \times 10^5$. In Figures 16, 17, 18, and 19, solid lines represent $Re = 7.5 \times 10^4$, dashed lines represent $Re = 1.0 \times 10^5$, and dotted lines represent $Re = 1.5 \times 10^5$. Lines of the same color have the same gap size.

Figures 16, 17, 18, and 19 show the effect of Reynolds numbers and gap sizes for various configurations of wingtip angles of attack, α_t, over a sweep of the base wing angle of attack, α_b, in the planar configuration. The $Re = 7.5 \times 10^4$ case stalled at a lower α_b than the other two Reynolds numbers tested, so tests for higher values of α_b were not conducted for the Reynolds number.

Qualitatively, Figures 16, 17, 18, and 19 show that changing the Reynolds number for a given configuration does not significantly change the relative trends for which gap size, γ, value provides the greatest amount of lift. In Figure 16, the $\gamma = 40\%$ configuration has the greatest C_{Lmax} when $Re = 7.5 \times 10^4$ and $Re = 1.0 \times 10^5$. When $Re = 1.5 \times 10^5$, the $\gamma = 20\%$ configuration produces only a 1% greater C_{Lmax} than the $\gamma = 40\%$ configuration, demonstrating that these values are very close. Likewise, in Figures 17 and 18, the $\gamma = 20\%$ configuration is dominant across all three tested Reynolds numbers.

In Figure 23, there is some variation in which γ value produces the most lift. At $Re = 7.5 \times 10^4$, $\gamma = 40\%$ produces the greatest C_{Lmax}, at $Re = 1.0 \times 10^5$, $\gamma = 0\%$ produces the greatest C_{Lmax}, and at $Re = 1.5 \times 10^5$, $\gamma = 20\%$ produces the greatest C_{Lmax}. Another noticeable factor in this dataset is that, unlike other wingtip angle of attack configurations,
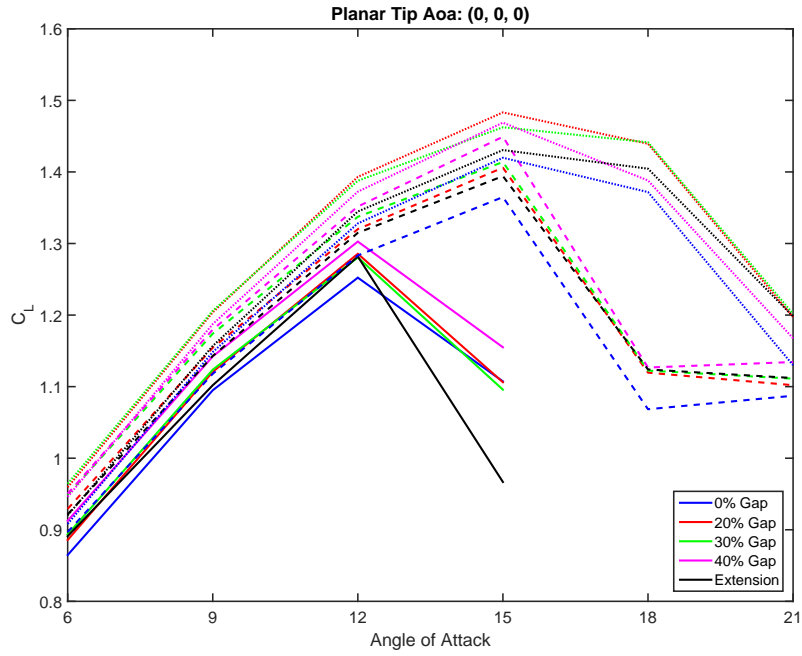
22

Figure 16: C_L vs α_b graph for α_t configuration (0, 0, 0) with varying gap sizes at three different Re.
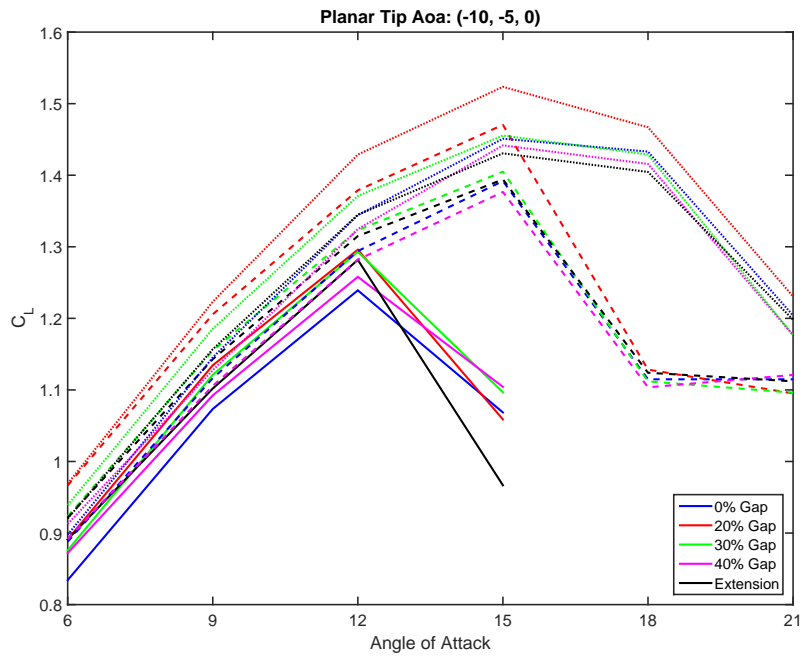

Figure 17: C_L vs α_b graph for α_t configuration (-10, -5, 0) with varying gap sizes at three different Re.
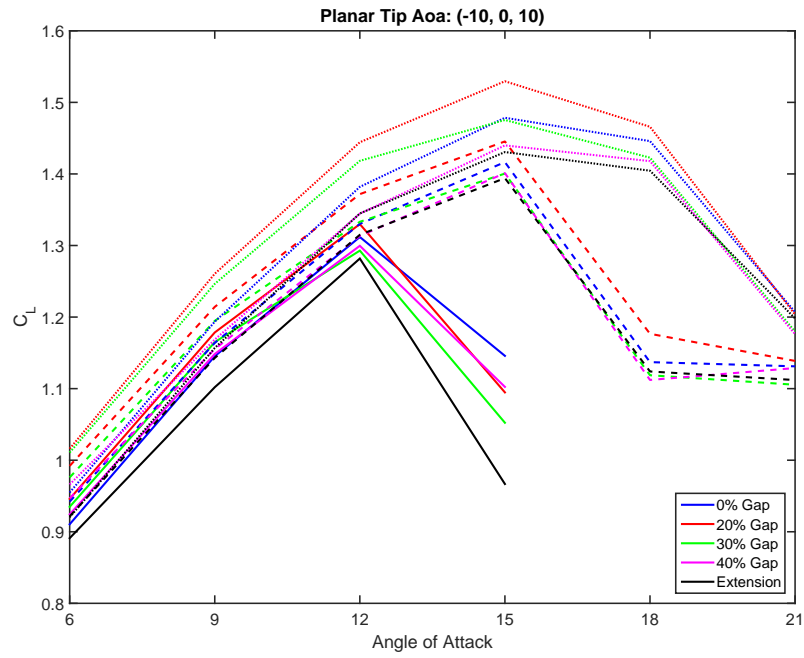
Figure 18: C_L vs α_b graph for α_t configuration (-10, 0, 10) with varying gap sizes at three different Re.
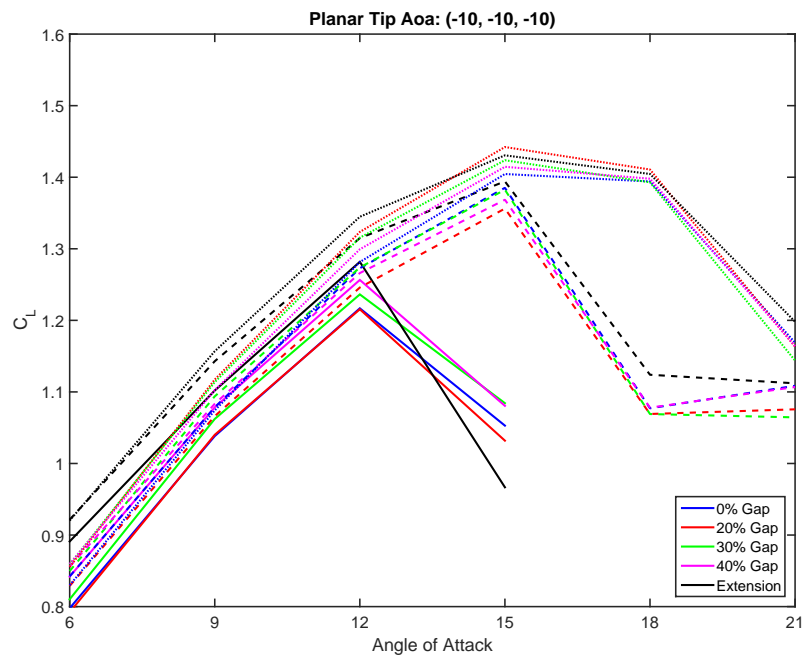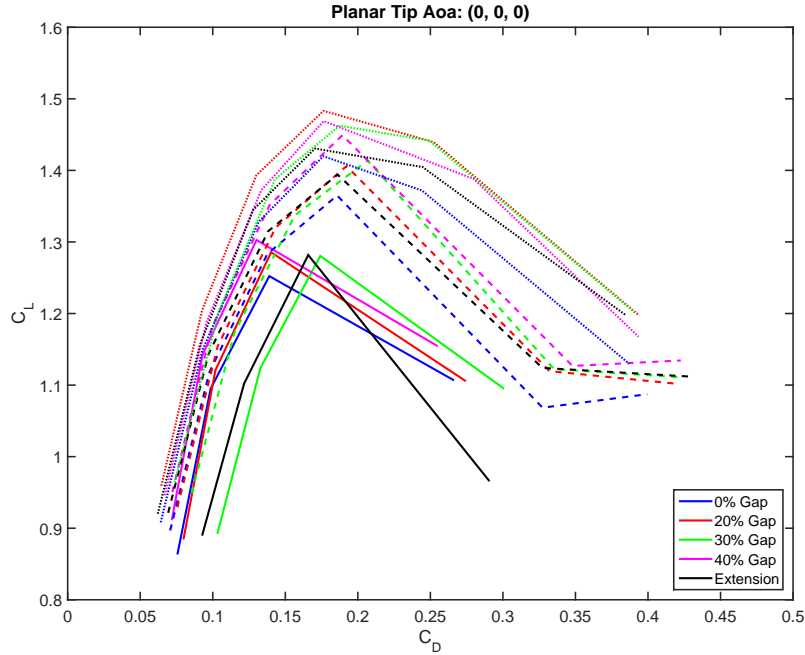

Figure 19: C_L vs α_b graph for α_t configuration (-10, -10, -10) with varying gap sizes at three different Re.

Figure 20: C_L vs C_D graph for α_t configuration (0, 0, 0) with varying gap sizes at three different Re.

this configuration of α_t generally produced a lower C_L than the wingtip extension at any value of γ. This is especially apparent in the $Re = 7.5 \times 10^4$ case and the $Re = 1.0 \times 10^5$ case where the wingtip extension produced a greater C_L value for a given α_b than any gap size in the pre-stall region where $6° \leq \alpha_b \leq 12°$ for the $Re = 7.5 \times 10^4$ case and $6° \leq \alpha_b \leq 15°$ for the other cases. When $Re = 1.5 \times 10^5$, the $\gamma = 20\%$ case was able to produce more lift than the wingtip extension, but only at C_{Lmax}.

Figures 20, 21, 22, and 23 plot C_L against C_D at the various configurations of α_t, showing the effects of varying γ and Re. Plotting C_L against C_D is a way to characterize the aerodynamic efficiency of a given configuration. In general, a more efficient design will produce less C_D for a given value of C_L, or in other words, the drag penalty for producing a desired amount of lift will be reduced.

At low Reynolds numbers, where $Re = 7.5 \times 10^4$, the effect of wingtip devices on C_D shows that $\gamma = 40\%$ incurs the lowest drag penalty. This is true across all configurations shown in Figures 20, 21, 22, and 23. Having a gap size of 0% also tends to incur a low drag penalty, especially in the (-10, -10, -10) configuration of α_t as seen in Figure 23. In general, these low Reynolds number tests show that having a simple wingtip extension or using gap sizes of 20% and 30% are generally detrimental to aerodynamic efficiency due to large drag penalties.
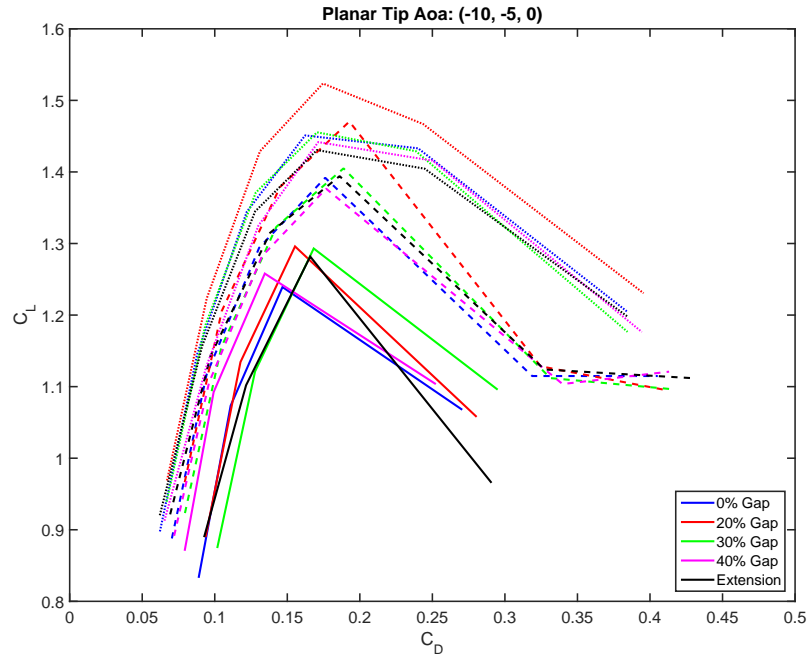
Figure 21: C_L vs C_D graph for α_t configuration (-10, -5, 0) with varying gap sizes at three different Re.
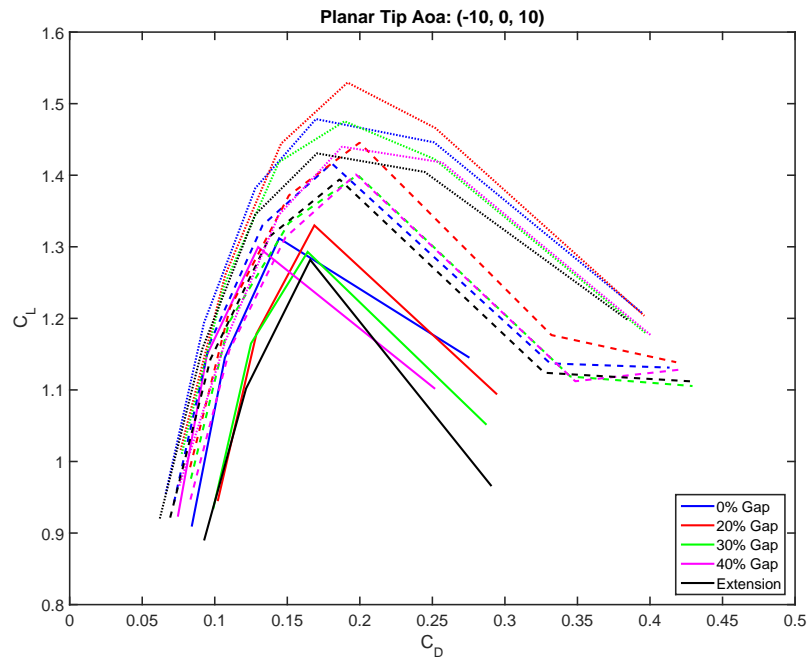

Figure 22: C_L vs C_D graph for α_t configuration (-10, 0, 10) with varying gap sizes at three different Re.
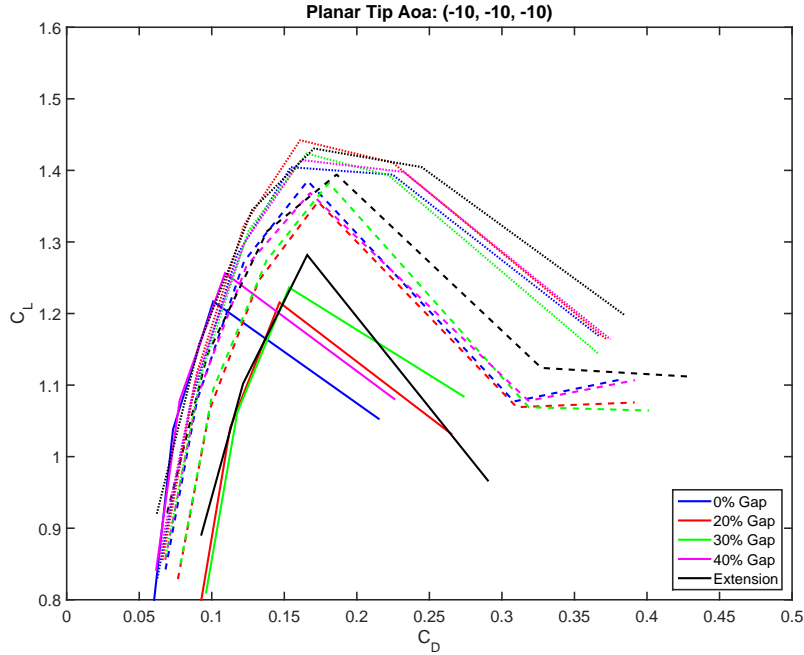
Figure 23: C_L vs C_D graph for α_t configuration (-10, -10, -10) with varying gap sizes at three different Re.

The relative trends between the plotted C_L vs C_D curves remain much more consistent at the higher tested Reynolds numbers of $Re = 1.0 \times 10^5$ and $Re = 1.5 \times 10^5$. In Figure 20, the 20% and 40% configurations of γ are generally the most efficient configurations, especially at higher values of C_L. The performance of the $\gamma = 40\%$ configuration drops off significantly when α_t is in the (-10, -5, 0) configuration or the (-10, 0, 10) configuration, becoming one of the least efficient configurations. However, the 20% gap size configuration remains the most efficient, especially at higher values of C_L. In fact, the $\gamma = 20\%$ configuration is able to produce more lift at $Re = 1.0 \times 10^5$ than some gap sizes are able to at $Re = 1.5 \times 10^5$, though this comes with a drag penalty due to operating at a lower Reynolds number, and therefore less efficient condition.

Figure 23 does not demonstrate the same, repeatable relative trends between C_L vs C_D curves for varying gap sizes at the higher two tested Reynolds numbers, $Re = 1.0 \times 10^5$ and $Re = 1.5 \times 10^5$. In this configuration, all of the gap sizes perform somewhat similarly, and which value of γ provides the greatest efficiency is very sensitive to Reynolds number. The most noticeable aspect of this dataset is that, at these two Reynolds numbers, a simple wingtip extension is nearly the most efficient configuration. Given the high sensitivity of γ at these Reynolds numbers, it would be more advisable to use a wingtip extension than to use wingtip gaps.
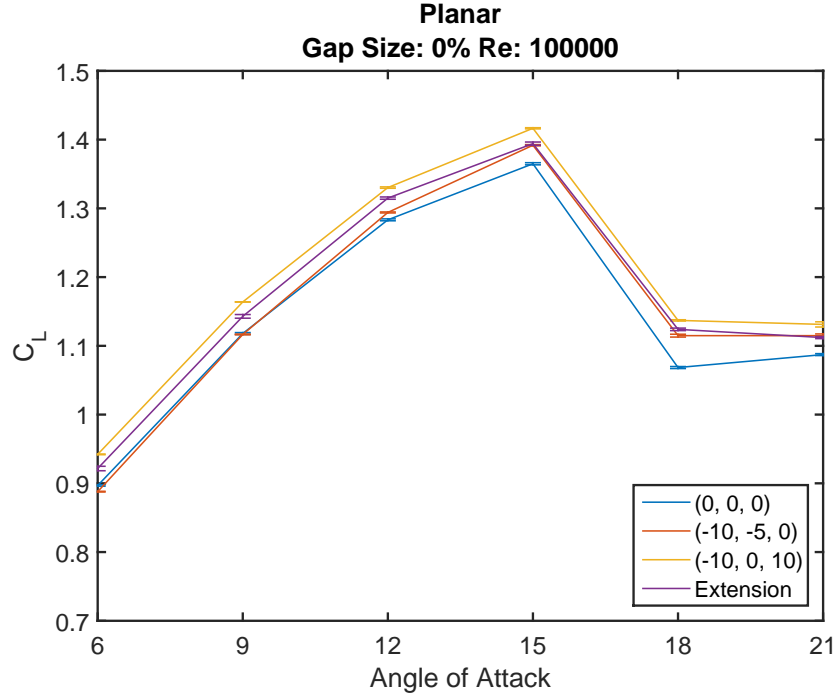
Figure 24: C_L vs α_b for the planar configuration demonstrating the effect of α_t. Here, the (0, 0, 0) configuration produces the lowest C_{Lmax}.

As stated in the introduction, the goal of this research is to produce efficient, high lift wingtip devices. In examining the experimental results shown in Figures 19 and 23, the (-10, -10, -10) configuration of α_t produces very little lift relative to other configurations and is a poor configuration for the goal of this study. It is often outperformed by a simple wingtip extension. Therefore, the remaining sections will omit an analysis of this configuration.

In examining the overall effects of Reynolds numbers on the remaining configurations, especially at $Re = 1.0 \times 10^5$ and $Re = 1.5 \times 10^5$, the relative trends of varying gap sizes remains largely the same. For the sake of simplicity, the remaining sections will focus the analysis on when the Reynolds number is 1.0×10^5. This Reynolds number corresponds to a bird with a chord length of 150 mm flying at approximately 10 m/s, a reasonable cruise speed for many species of hawks and falcons [28].

4.2   Effect of Wingtip Angle of Attack

The data shown in Figures 24, 25, 26, and 27 demonstrate the effect of the wingtip angles of attack, α_t as defined in Table 1, on the coefficient of lift over an angle of attack sweep for the planar configuration. Figure 28 shows the effect of α_t on the coefficient of lift over an angle of attack sweep for the nonplanar configuration. The error bars in these figures show
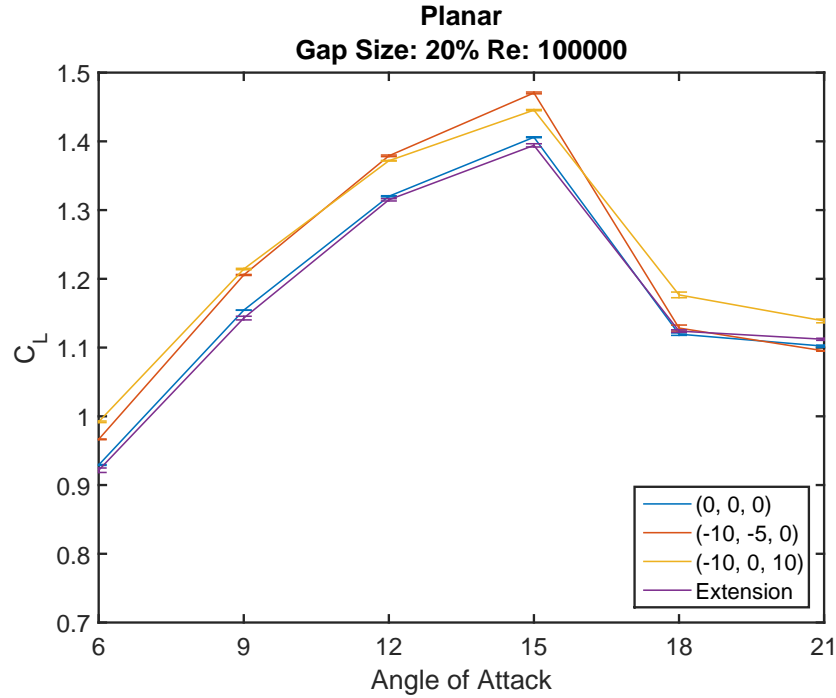
Figure 25: C_L vs α_b for the planar configuration demonstrating the effect of α_t. The (-10, -5, 0) configuration produces the greatest C_{Lmax} among all configurations. This was the highest recorded value for C_{Lmax} tested.
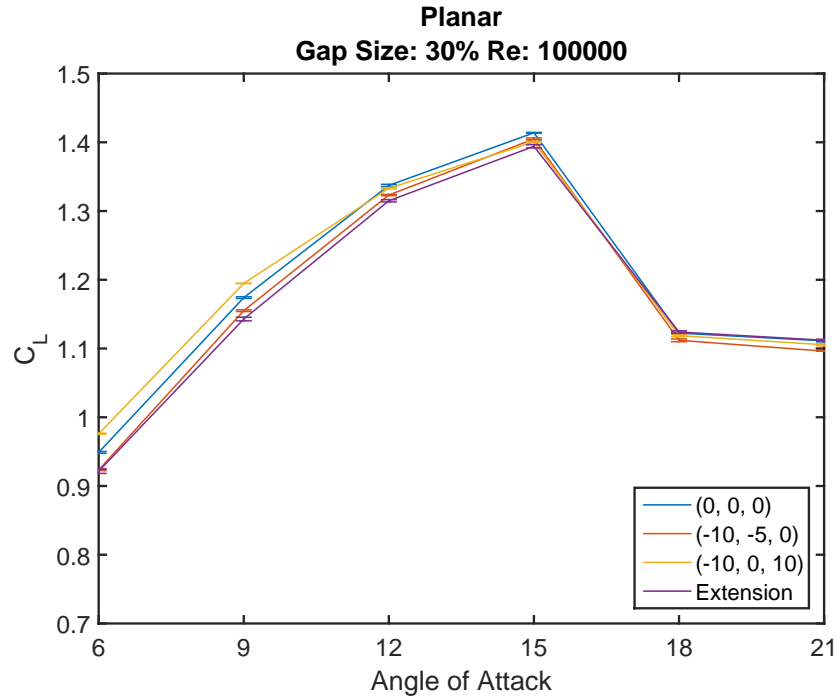

Figure 26: C_L vs α_b for the planar configuration demonstrating the effect of α_t. The performance of the (-10, -5, 0) and (-10, 0, 10) configurations is diminished.
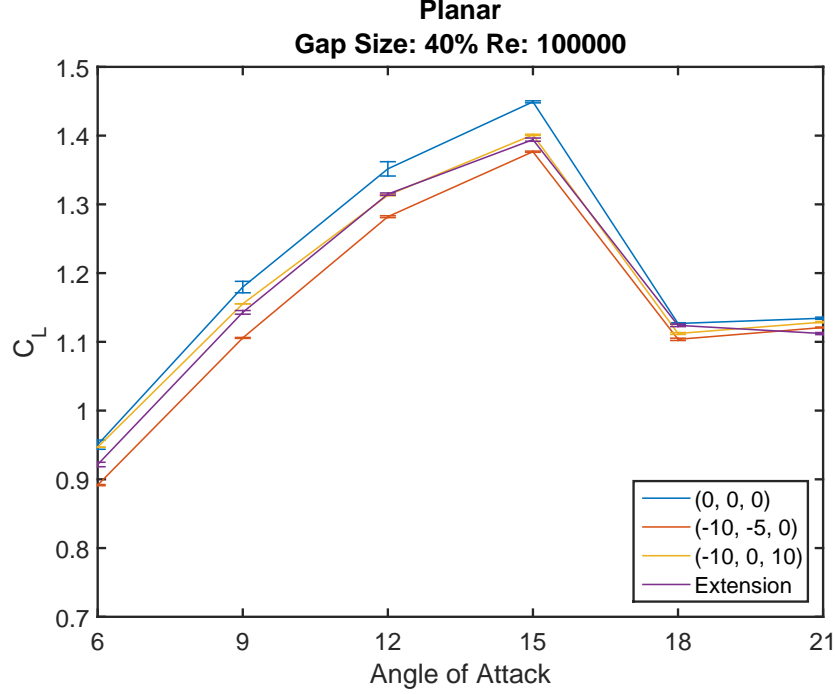
Figure 27: C_L vs α_b for the planar configuration demonstrating the effect of α_t. The (0, 0, 0) configuration produces the highest C_{Lmax} at this gap size.

the standard error of the data over multiple test runs.

In the planar configuration with $\gamma = 0\%$, shown in Figure 24, the (0, 0, 0) configuration for α_t provides the lowest C_{Lmax} whereas the (-10, 0, 10) configuration provides the greatest C_{Lmax}. The benefits to C_{Lmax} becomes even more significant when $\gamma = 20\%$ as seen in Figure 25. At this gap size, the (-10, -5, 0) configuration produces a 4.39% increase in the mean C_L in the pre-stall region, where $6° \leq \alpha_b \leq 15°$, and a 4.55% increase in C_{Lmax} as compared with the (0, 0, 0) configuration. The 20% gap size configuration produces the greatest C_{Lmax} when compared to all gap sizes tested.

In Figures 26 and 27, C_{Lmax} and the mean C_L over the pre-stall region for the (-10, -5, 0) and the (-10, 0, 10) configurations are reduced as γ increases. The (0, 0, 0) configuration continues to have an increased C_{Lmax}, however, even at its peak, as seen in Figure 27, it does not outperform the (-10, -5, 0) configuration at $\gamma = 20\%$. From these graphs, it is clear that the planar wingtip configurations are sensitive to α_t, which agrees with Graham's findings and Fluck and Crawford's conclusion [14, 27]. As Graham explained, the wingtips of birds are offset at various angles of attacks which allows the wingtips to change the direction of the freestream flow. Depending on the exact angles of attack in a given configuration, it is expected that the flow direction will be turned differently with varying degrees of efficiency.

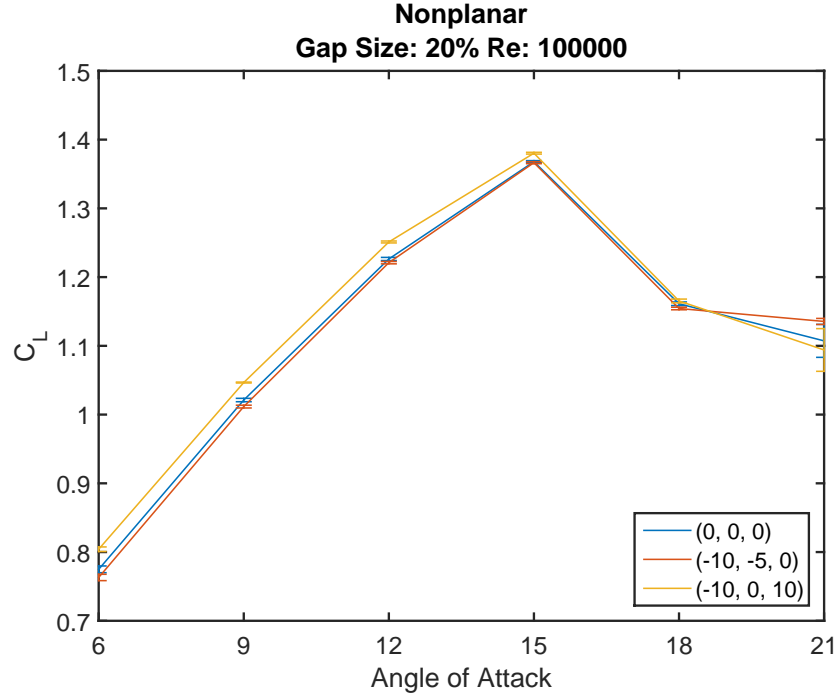In contrast to the findings for the planar configuration, Figure 28 shows that, for the

Figure 28: C_L vs α_b for the nonplanar configuration demonstrating the effect of α_t. The lift curves have converged.

tested α_t, the lift curves converge. Similar results were found for other values of γ. There is no significant difference between the lift curves for the (0, 0, 0) and (-10, -5, 0) configurations. The (-10, 0, 10) configuration does show some improvement over the (0, 0, 0) configuration, with an overall increase in mean C_L of 2.31% across the pre-stall values of α_b, however, the difference in C_{Lmax} is less than 1%. Overall, it appears that nonplanar wingtip devices are insensitive to changes in α_t, especially as compared with the planar wingtip devices.

Figures 29 and 30 show the coefficient of lift plotted against the coefficient of drag for the configurations of α_t described in Table 1 in both the planar and nonplanar configurations. Similar to Figures 25 and 28, these graphs show that the planar configuration is sensitive to the wingtip angle of attack configuration with (-10, -5, 0) having the greatest C_{Lmax}. Figure 29 also shows that, by changing the wingtip angle of attack configuration, large benefits to C_L can be obtained with minimal C_D penalties. The nonplanar configurations are once again insensitive to the wingtip angle of attack configurations and are virtually indistinguishable from each other.

Based on the findings above, the remainder of the analysis will focus on the (-10, -5, 0) configuration for α_t since this configuration is the one that produces the greatest C_{Lmax} of any configuration.
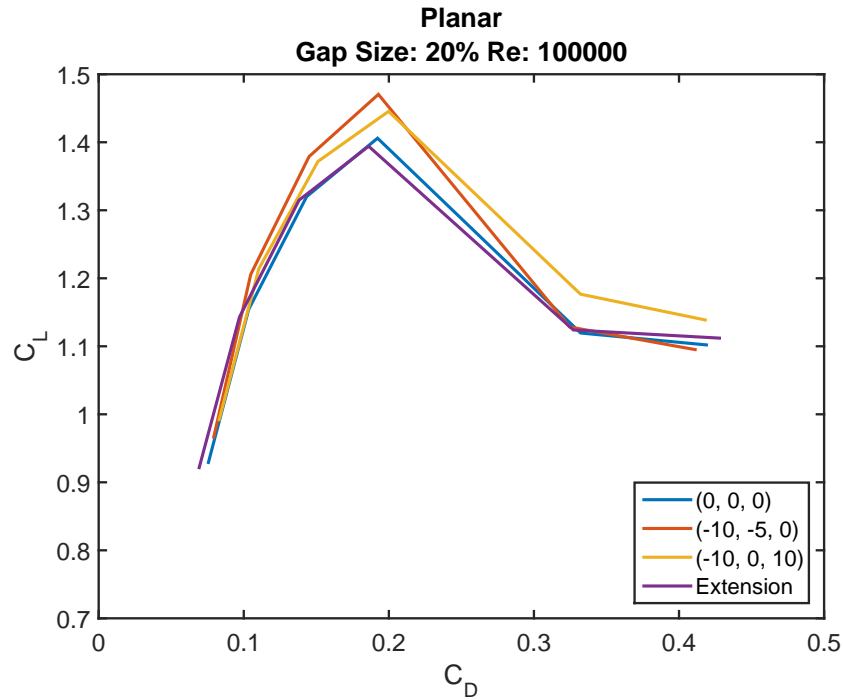
Figure 29: C_L vs C_D for the planar configuration demonstrating the effect of α_t. The (-10, -5, 0) configuration produces more C_L for a very minimal C_D penalty.
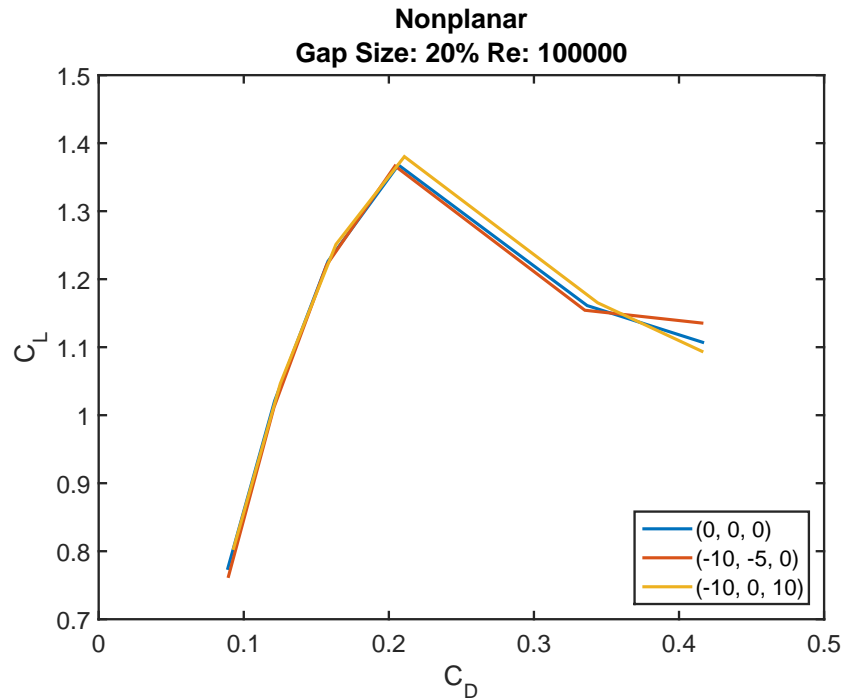

Figure 30: C_L vs C_D for the nonplanar configuration demonstrating the effect of α_t. The curves are virtually indistinguishable from each other, showing a reduced effect of α_t configurations in the nonplanar case.
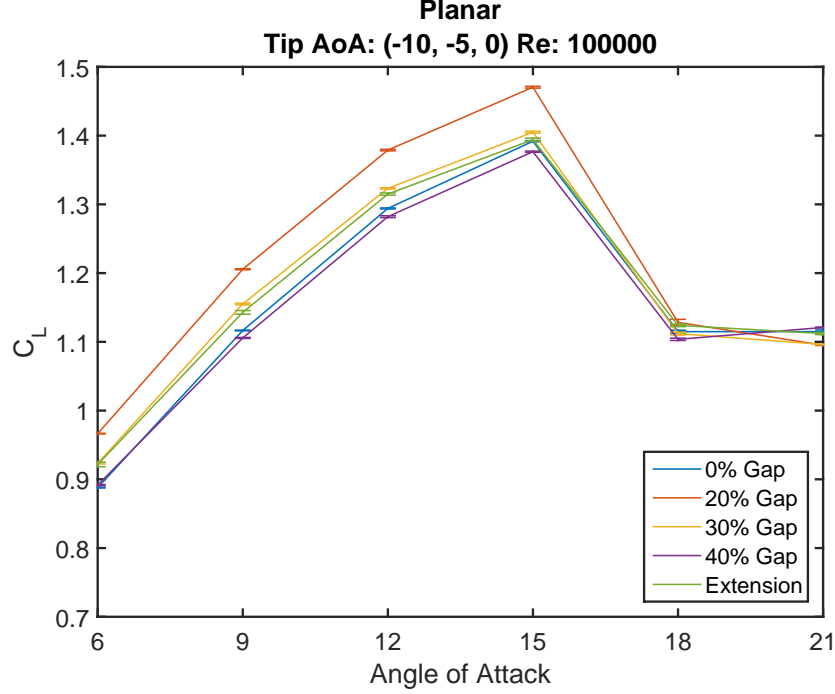
Figure 31: C_L vs α_b for the planar configuration demonstrating the effect of gap size. Varying γ has a large effect on C_L, and choosing $\gamma = 20\%$ provides the greatest increase in C_L across all α_b tested in the pre-stall region.

4.3 Effect of Wingtip Gaps

In analyzing the effect of gaps, both Figures 31 and 32 show that there is an improvement in C_L and especially in C_{Lmax} when $\gamma = 20\%$ over the baseline case of $\gamma = 0\%$ as well as the wingtip extension. For the planar condition, a γ value corresponding to 20% shows a 5.60% improvement in C_{Lmax} over the $\gamma = 0\%$ case and a 5.45% improvement over the wingtip extension. Over the entire range of C_L in the tested pre-stall region, the mean C_L for $\gamma = 20\%$ is 7.25% higher than when $\gamma = 0\%$ and 5.18% higher as compared with the wingtip extension. For the nonplanar condition, at $\gamma = 20\%$, C_{Lmax} increases by 3.48% and the overall C_L curve is 2.04% higher than for when $\gamma = 0\%$ in the pre-stall region.

However, when γ is increased beyond 20%, there is a reduction in the C_L curves. In the planar case, the reduction is gradual with $\gamma = 30\%$ still having a higher C_{Lmax} than either the wingtip extension or the $\gamma = 0\%$ case. However, once $\gamma = 40\%$, C_{Lmax} is lower than all other cases. For the nonplanar case, shown in Figure 32, an increase in gap size to 30% or 40% corresponds with a reduction in C_L across all α_b, and the C_L curves converge.

Figures 33 and 34 shows the coefficient of lift plotted against the coefficient of drag for both the planar and nonplanar configurations at various gap sizes and $\alpha_t = $ (-10, -5, 0). The C_L vs C_D curves shown in Figure 33 demonstrates that, when $\gamma = 20\%$, the wing-wingtip
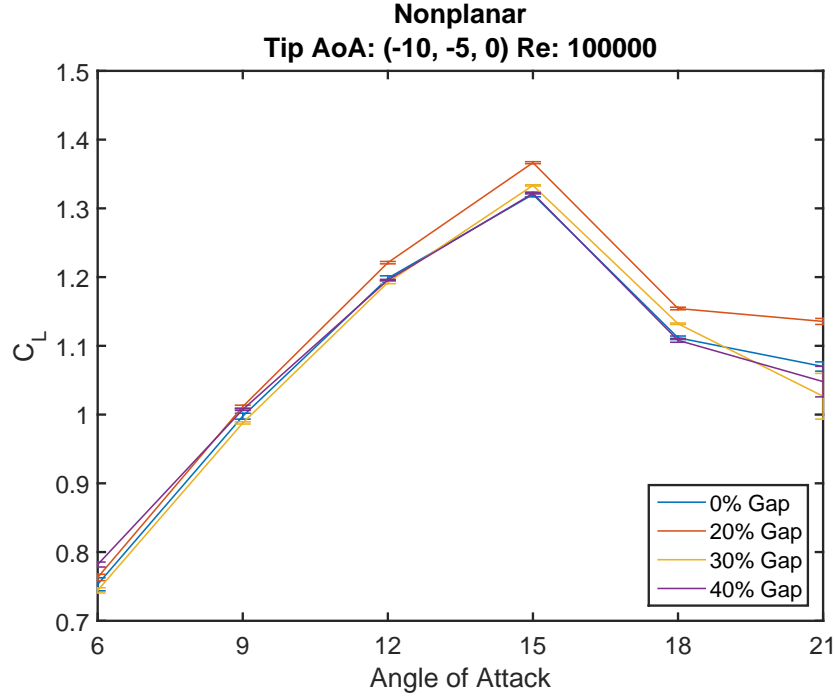
33

Figure 32: C_L vs α_b for the nonplanar configuration demonstrating the effect of gap size. Changing γ has a reduced effect on C_L, though $\gamma = 20\%$ still provides the greatest benefit to C_L and particularly to C_{Lmax}.

system is operating near peak efficiency. For this configuration, the wingtips generate a larger C_L all while either maintaining C_D, or, in some cases, reducing C_D for a given C_L. In particular, C_{Lmax} is significantly increased for $\gamma = 20\%$ as compared with all other planar configurations while suffering a very minimal C_D increase. Figure 33 also shows that when γ is increased beyond 20%, there is a detrimental effect to C_{Lmax}. In Figure 34, the benefits of using a gap size of 20% is reduced. Figure 34 shows a right shift in all of the efficiency curves for when $\gamma > 0\%$, signifying that for the nonplanar case, there is an increase in drag suffered when gaps are present.

$\gamma = 20\%$ shows the greatest improvement in C_L. These results are consistent in both the planar and nonplanar wingtip cases. Thus, the effects of wingtip gaps can be decoupled from the planarity of the wingtip geometry.

4.4 Effect of Wingtip Planarity

Figure 35 shows a plot of C_L over a sweep of α_b for the wingtip extension, planar, and nonplanar configurations where $\gamma = 20\%$ and the (-10, -5, 0) configuration of α_t was used. The nonplanar configuration generated less lift than both the planar configuration and the wingtip extension in the pre-stall region. C_{Lmax} was reduced by 7.07% and the average
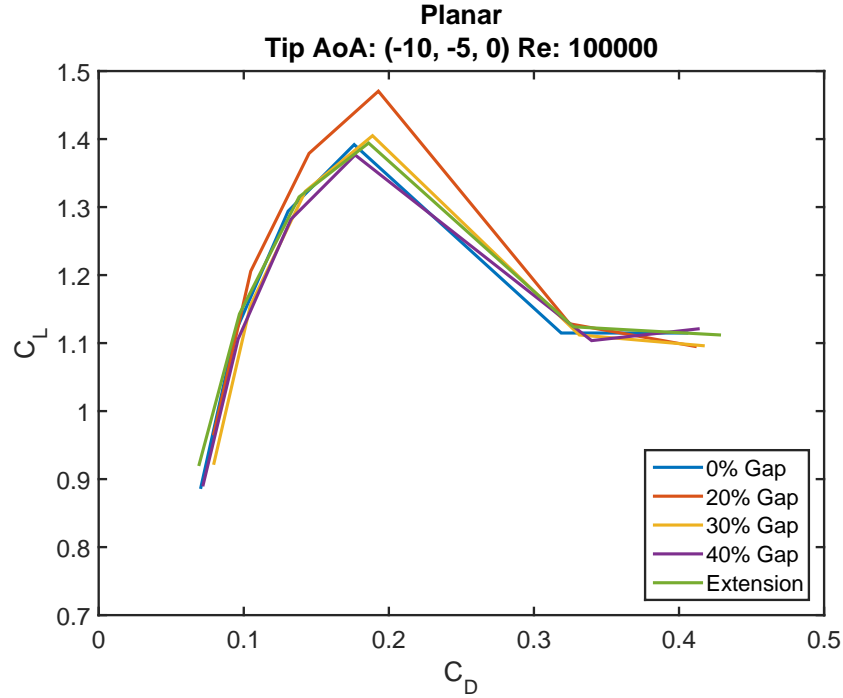
Figure 33: C_L vs C_D for the planar configuration demonstrating the effect of gap size. $\gamma = 20\%$ provides the greatest benefit to the aerodynamic efficiency of the wing-wingtip system, increasing C_L for a given C_D.
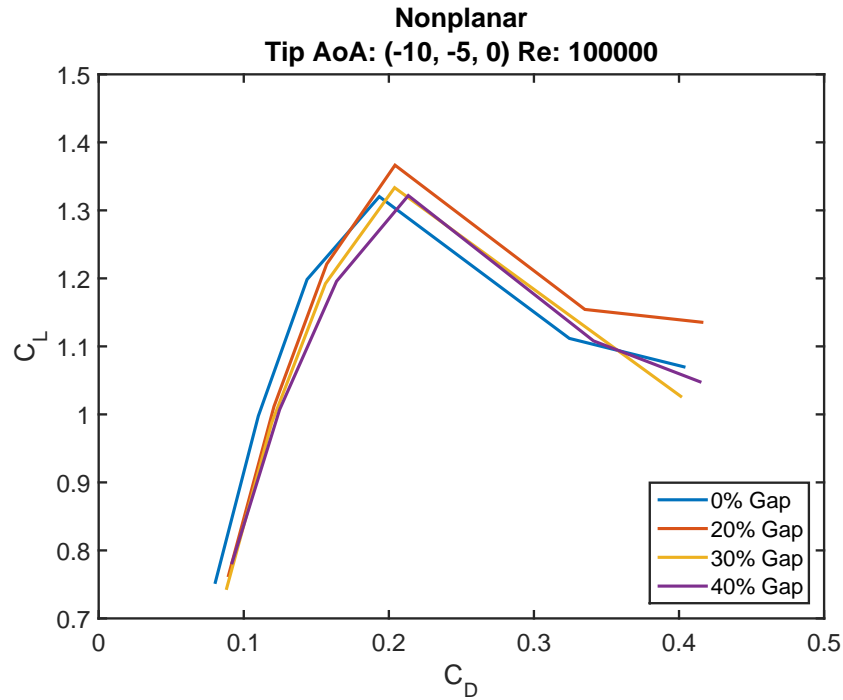

Figure 34: C_L vs C_D for the nonplanar configuration demonstrating the effect of gap size. The presence of wingtip gaps leads to a right shift in the C_L vs C_D curves, leading to a drag penalty for having gaps in the nonplanar configuration.
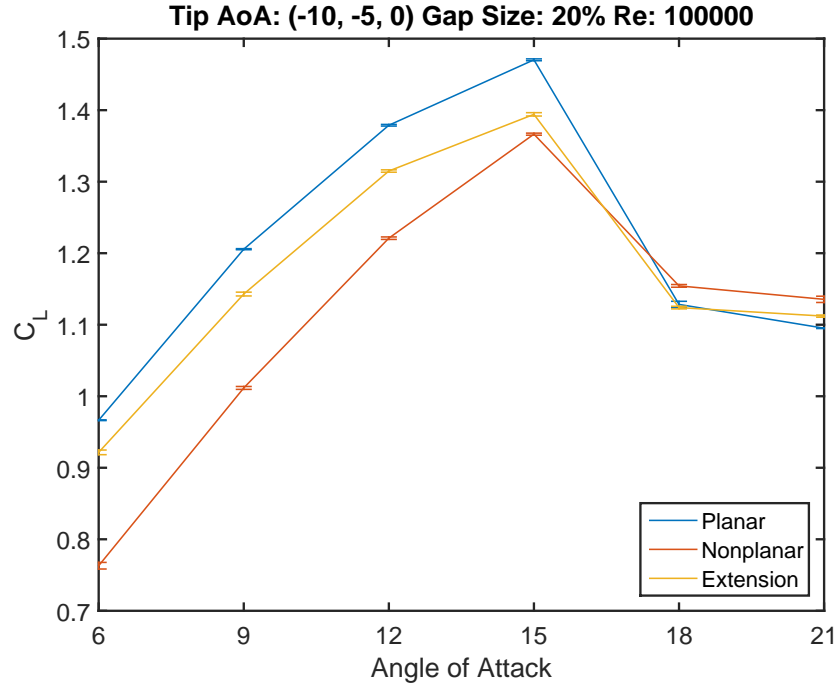
Figure 35: C_L vs α_b demonstrating the effect of planarity. The nonplanar configuration produces significantly less lift than both the wingtip extension and the planar configuration.

reduction in C_L across the pre-stall region was 13.92% as compared with the planar configuration. When the nonplanar configuration was compared with the wingtip extension, C_{Lmax} was reduced by only 2.01% and C_L was reduced by 9.44%.

Figure 36 plots C_L against C_D for the wingtip extension, planar, and nonplanar configurations where $\gamma = 20\%$ and α_t corresponded with the (-10, -5, 0) configuration. This graph shows that the nonplanar wingtip devices, in the configurations tested, do not improve aerodynamic efficiency, but instead cause a right shift in the C_L versus C_D curve.

These results show that the nonplanar configuration tested was less effective at producing lift and also less efficient than the planar configuration or the wingtip extension. These results cannot be generalized to state that all nonplanar configurations are less efficient than planar configurations, and instead, indicate that the designed nonplanar configuration used in this experiment is less efficient than a comparable planar configuration. In general though, nonplanar configurations can be more efficient as seen in the use of various nonplanar wingtip devices [9, 10, 12, 14–17].
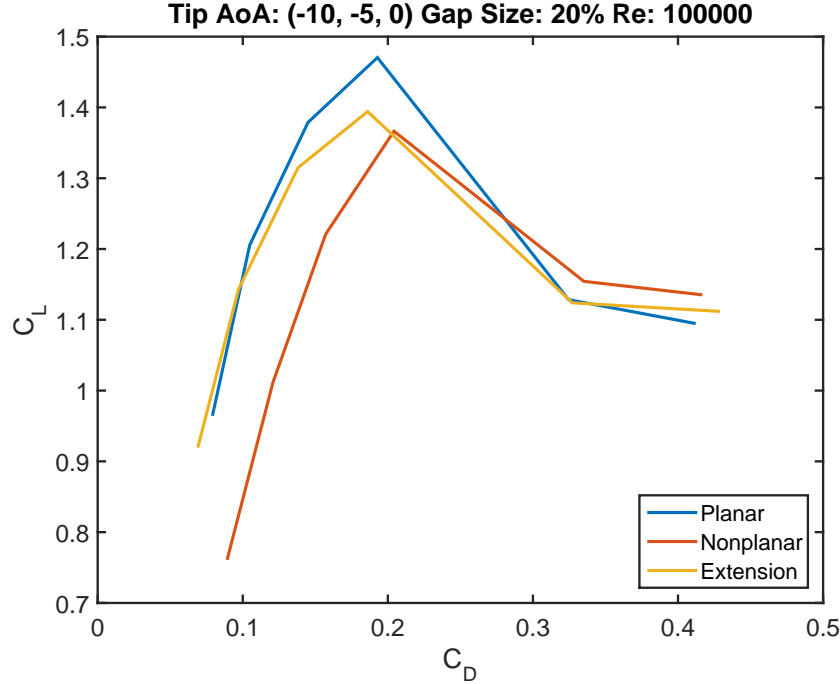
Figure 36: C_L vs C_D demonstrating the effect of planarity. The nonplanar configuration suffers a large drag penalty as compared with the planar configuration and the wingtip extension.

4.5 Induced Drag

To understand the effects of the wingtip devices on drag, drag must first be broken down into components of induced drag and profile drag as shown in Equation 8. Other components of drag, such as wave drag, can be ignored due to the low Reynolds number [29].

$$C_D = C_{Dpr} + C_{Di} \tag{8}$$

Profile drag is defined as the total of the skin friction drag and form drag for a two-dimensional airfoil section. Skin friction is the component of drag resulting from viscous shearing stresses over the wetted surface of the airfoil surface. Form drag, sometimes referred to as pressure drag, is defined as the drag resulting from the integrated effect of the static pressure acting normal to its surface resolved in the drag direction [29].

In contrast to these forms of drag, induced drag is the drag due to lift that results from the generation of trailing vortices [29] and is defined in Equation 9.

$$C_{Di} = \frac{C_L^2}{\pi ARe} \tag{9}$$

To calculate C_{Di}, the Oswald's efficiency factor, e, was approximated from Figure 4.21
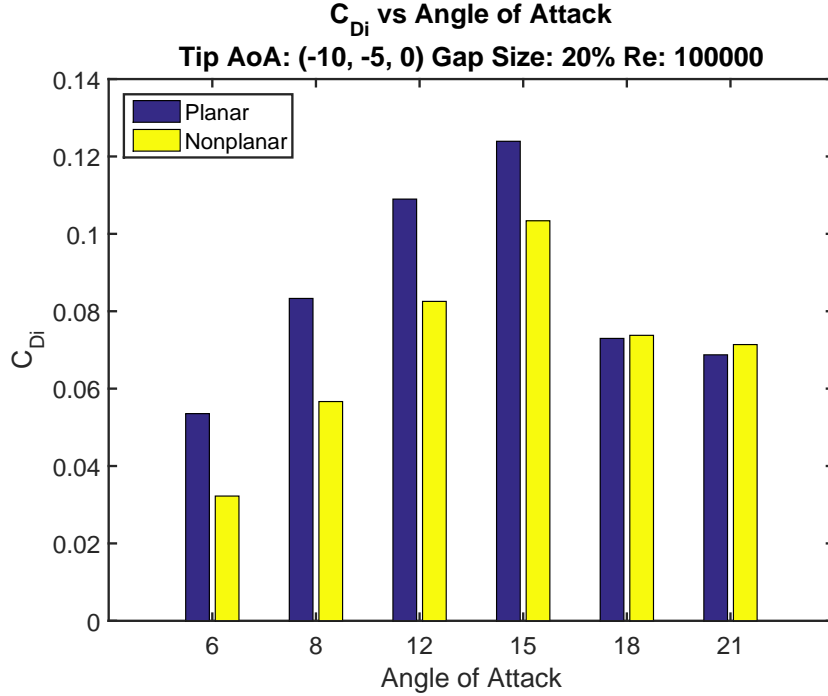
Figure 37: C_{Di} vs α_b for planar and nonplanar configurations showing a reduction in induced drag when switching to a nonplanar configuration.

in [29] for the planar configuration. For the nonplanar configuration, modifications to the Oswald's efficiency factor had to be made in accordance with Equation 10 derived in [30].

$$C_{Di} = \frac{C_L^2}{\pi A R e_{wl}} \tag{10}$$

The new Oswald's efficiency factor, e_{wl}, takes into account the geometry of the winglets. The value can be calculated from Equation 11.

$$e_{wl} = \left(1 + \frac{2}{k_{wl}}\frac{h}{b}\right)^2 e \tag{11}$$

In this equation, h is the height of the winglets and b is the total wingspan. This equation tends to overestimate the benefits of winglets, and Niţă [30] proposed the addition of a penalty factor, k_{wl} which took into account the effectiveness of a winglet. If the additional height of a winglet were to work identically to a span increase, then $k_{wl} = 1$. Using data from Kroo's work, Niţă estimated $k_{wl} = 2.13$ for a similar configuration [11, 30].

Figure 37 presents the calculated values of C_{Di} for the (-10, -5, 0) configuration of α_t with $\gamma = 20\%$ for both the planar and nonplanar configurations. This graph shows that, in the pre-stall region, the induced drag is reduced by 16.55% to 39.78% by switching to the nonplanar configuration.
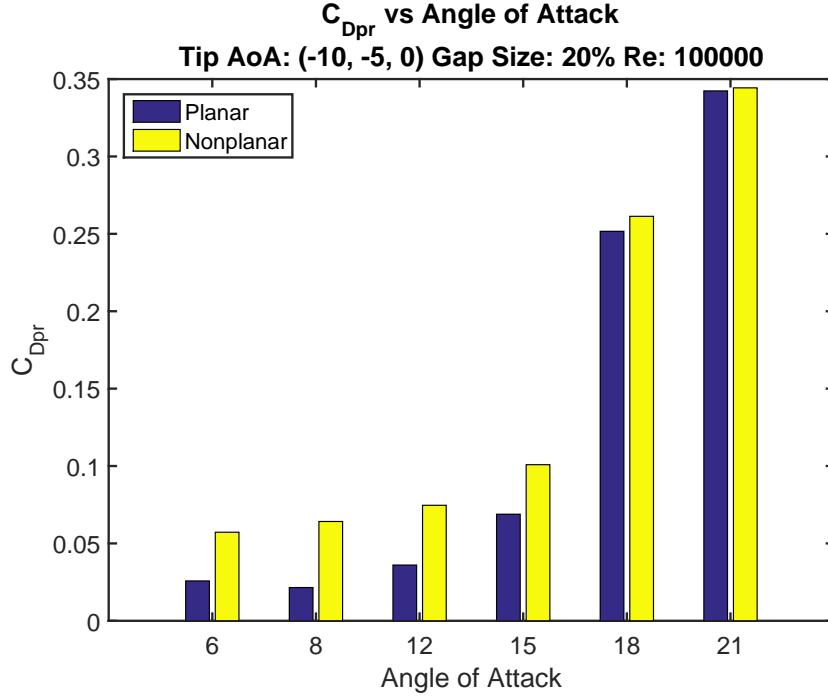
Figure 38: C_{Dpr} vs α_b for planar and nonplanar configurations showing an increase in profile drag when switching to a nonplanar configuration.

Figure 38 shows the calculated values of C_{Dpr} for the (-10, -5, 0) configuration with $\gamma = 20\%$ in both the planar and nonplanar configurations. This graph demonstrates that, by switching to the nonplanar configuration, there is an additional C_{Dpr} penalty suffered.

To understand the context of Figures 37 and 38, it is important to understand the design considerations for winglets. The goal of winglet design is to optimize the winglet geometry such that a maximum reduction in C_{Di} and minimum increase in C_{Dpr} can be achieved, thereby resulting in the lowest possible C_D. The winglets used in this experiment were able to significantly reduce C_{Di} as shown previously in Figure 37, however, this was coupled with an even larger increase in C_{Dpr}.

The focus of this research is not on optimal winglet design, but instead demonstrating that these wingtip devices are capable of reducing C_{Di}. Further design iterations can focus on improving the design of the nonplanar wingtip devices to further increase C_L/C_D and minimize the C_{Dpr} penalty suffered.

4.6   Summary of Experimental Results

In summary, the lift and drag data collected yielded many interesting and useful results. In the planar configuration, the experiments show that the wing has very different per-

formance levels at the different tested Reynolds numbers, but the relative trends between various wingtip gap sizes, γ, remains unchanged. For many configurations, the $\gamma = 20\%$ gap size provides the greatest C_{Lmax} and the most aerodynamically efficient operating configuration. The experiment also shows that planar wingtip gaps were sensitive to α_t whereas the nonplanar configurations were not.

In examining the effect of wingtip gaps, results show that, for a planar wing with $\gamma = 20\%$ at $Re = 1.0 \times 10^5$, the mean C_L increased by 7.25%, and C_{Lmax} was increased by 5.60% as compared to a wing without wingtip gaps, where $\gamma = 0\%$. The nonplanar configuration also shows an improvement of C_L and C_{Lmax} when the wingtip gaps were deployed to $\gamma = 20\%$.

The nonplanar wingtip devices reduced the induced drag of the wing, however, this came at a cost of increased profile drag. With a different design of nonplanar wingtip devices, the induced drag could be reduced without such a large profile drag penalty, thus making the nonplanar design viable.

A morphing mechanism design, enabled by a bistable structure and SMA coil actuator, was investigated, and a design process was proposed. Following this design process will enable the development of an actively controlled wingtip device that can adjust the wingtip gaps to be either 0% or 20%.

5 Conclusions and Future Work

5.1 Conclusions

Lift and drag data were experimentally obtained for a proposed wingtip device employing wingtip gaps as shown in Figure 1. For the configurations and Reynolds numbers tested, the $\gamma = 20\%$ gap size consistently generated the most lift. The effects of varying γ were shown to not be strongly related to the planarity of the wingtip device. In essence, the wingtip gap effects can be decoupled from the planarity effects in the design of similar wingtip device, where wingtip gaps had a favorable effect on lift while wing non-planarity has a favorable effect on induced drag. Decoupling these two effects will allow designers to take advantage of the properties of both parameters, enabling the design of a high lift, low drag wing system at low Reynolds numbers.

By incorporating the proposed morphing mechanism, a small UAV would be able to take advantage of benefits of both the no gap configuration as well as the 20% gap size configuration, all while adding very little weight to the system. The morphing mechanism takes advantage of the bistable structure and allows for the use of smaller and lighter weight SMA coil actuators that would not have been possible otherwise. This device will enable increased mission adaptability by allowing UAVs to deploy the gaps in conditions such as takeoff where, due to payload requirements, increased C_L is required while also allowing a UAV to close wingtip gaps during cruise conditions to reduce drag penalties.

5.2 Future Work

There are many avenues for future work that can be done with this project. For example, a more in depth aerodynamic analysis can be performed on the planar system to determine the optimal wingtip angles of attack for various Reynolds numbers and base wing angles of attack. To determine optimal wingtip configurations, one approach would be to use a low fidelity solver in the pre-stall region such as a vortex lattice code. A large variety of wingtip angles could be tested very quickly, and the best candidates could then be confirmed using a full CFD approach.

Another possible avenue for future work would be to improve the nonplanar winglet geometry. The results from the performed experiments showed that nonplanar wingtips are beneficial, but that the wingtips need to be carefully designed, optimizing the geometry of the nonplanar winglets to minimize the profile drag penalty and maximize the reduction in induced drag.

Aside from pure aerodynamics, iterative work should be done to refine the morphing

mechanism proposed in this research to optimize the design for specific flight requirements. Work can also be done on designing an adaptive wingtip with an addition degree of freedom that can dynamically vary γ and α_t under a variety of flight conditions to improve performance. The bistable structure explored in this experiment provides the basis for varying γ, but work could be done to add an additional degree of freedom for α_t to vary. Utilizing a combined passive-active approach would allow for reduced energy consumption when passively adapting to environmental conditions while also allowing for direct control over some of the wing geometry in an active manner to compensate for environmental conditions. Moreover, these adaptive wingtip devices can be used for yaw stability and aircraft control, as suggested by [31] and [32], respectively.

6   References

[1] B. W. Tobalske, "Biomechanics and physiology of gait selection in flying birds," *Physiological and Biochemical Zoology*, vol. 73, no. 6, pp. 736–750, 2000.

[2] A. Mohamed, K. Massey, S. Watkins, and R. Clothier, "The attitude control of fixed-wing mavs in turbulent environments," *Progress in Aerospace Sciences*, vol. 66, pp. 37–48, 2014.

[3] S. Miley, "On the design of airfoils for low reynolds numbers," in *2nd International Symposium on the Technology and Science of Low Speed and Motorless Flight*, p. 1017, 1974.

[4] P. C. Withers, "An aerodynamic analysis of bird wings as fixed aerofoils," *Journal of Experimental Biology*, vol. 90, no. 1, pp. 143–162, 1981.

[5] G. K. Taylor, A. C. Carruthers, T. Y. Hubel, and S. M. Walker, "Wing morphing in insects, birds and bats: mechanism and function," *Morphing Aerospace vehicles and structures*, pp. 11–40, 2012.

[6] V. A. Tucker, "Drag reduction by wing tip slots in a gliding harris' hawk, parabuteo unicinctus," *Journal of Experimental Biology*, vol. 198, no. 3, pp. 775–781, 1995.

[7] D. Savile, "Adaptive evolution in the avian wing," *Evolution*, pp. 212–224, 1957.

[8] S. Watkins, J. Milbank, B. J. Loxton, and W. H. Melbourne, "Atmospheric winds and their implications for microair vehicles," *AIAA journal*, vol. 44, no. 11, pp. 2591–2600, 2006.

[9] I. Kroo, "Drag due to lift: concepts for prediction and reduction," *Annual Review of Fluid Mechanics*, vol. 33, no. 1, pp. 587–617, 2001.

[10] R. T. Whitcomb, "A design approach and selected wind tunnel results at high subsonic speeds for wing-tip mounted winglets," 1976.

[11] I. Kroo, "Nonplanar wing concepts for increased aircraft efficiency," *VKI lecture series on innovative configurations and advanced concepts for future civil aircraft*, pp. 6–10, 2005.

[12] D. McLean, "Wingtip devices: What they do and how they do it," in *Boeing Performance and Flight Operations Engineering Conference*, 2005.

[13] U. La Roche and S. Palffy, "Wing-grid, a novel device for reduction of induced drag on wings," in *ICAS PROCEEDINGS*, vol. 20, pp. 2303–2309, 1996.

[14] M. Fluck and C. Crawford, "A lifting line model to investigate the influence of tip feathers on wing performance," *Bioinspiration & biomimetics*, vol. 9, no. 4, p. 046017, 2014.

[15] H. D. Cern-Muoz and F. M. Catalano, "Experimental analysis of the aerodynamic characteristics adaptive of multi-winglets," *Proceedings of the Institution of Mechanical Engineers, Part G: Journal of Aerospace Engineering*, vol. 220, no. 3, pp. 209–215, 2006.

[16] J. E. Guerrero, D. Maestro, and A. Bottaro, "Biomimetic spiroid winglets for lift and drag control," *Comptes Rendus Mecanique*, vol. 340, no. 1-2, pp. 67–80, 2012.

[17] M. Smith, N. Komerath, R. Ames, O. Wong, and J. Pearson, "Performance analysis of a wing with multiple winglets," in *19th AIAA Applied Aerodynamics Conference*, p. 2407, 2001.

[18] G. J. Simitses and D. H. Hodges, *Fundamentals of structural stability*. Butterworth-Heinemann, 2006.

[19] S. Shan, S. H. Kang, J. R. Raney, P. Wang, L. Fang, F. Candido, J. A. Lewis, and K. Bertoldi, "Multistable architected materials for trapping elastic strain energy," *Advanced Materials*, vol. 27, no. 29, pp. 4296–4301, 2015.

[20] C. S. Haines, M. D. Lima, N. Li, G. M. Spinks, J. Foroughi, J. D. Madden, S. H. Kim, S. Fang, M. J. de Andrade, F. Göktepe, *et al.*, "Artificial muscles from fishing line and sewing thread," *science*, vol. 343, no. 6173, pp. 868–872, 2014.

[21] S. M. Mirvakili, A. R. Ravandi, I. W. Hunter, C. S. Haines, N. Li, J. Foroughi, S. Naficy, G. M. Spinks, R. H. Baughman, and J. D. Madden, "Simple and strong: Twisted silver painted nylon artificial muscle actuated by joule heating," in *SPIE Smart Structures and Materials+ Nondestructive Evaluation and Health Monitoring*, pp. 90560I–90560I, International Society for Optics and Photonics, 2014.

[22] S. Kim, E. Hawkes, K. Choy, M. Joldaz, J. Foleyz, and R. Wood, "Micro artificial muscle fiber using niti spring for soft robotics," in *Intelligent Robots and Systems, 2009. IROS 2009. IEEE/RSJ International Conference on*, pp. 2228–2234, IEEE, 2009.

[23] B. Holschuh and D. Newman, "Low spring index, large displacement shape memory alloy (sma) coil actuators for use in macro-and micro-systems," in *SPIE MOEMS-MEMS*, pp. 897505–897505, International Society for Optics and Photonics, 2014.

[24] S. Seok, C. D. Onal, K.-J. Cho, R. J. Wood, D. Rus, and S. Kim, "Meshworm: a peristaltic soft robot with antagonistic nickel titanium coil actuators," *IEEE/ASME Transactions on mechatronics*, vol. 18, no. 5, pp. 1485–1497, 2013.

[25] S.-M. An, J. Ryu, M. Cho, and K.-J. Cho, "Engineering design framework for a shape memory alloy coil spring actuator using a static two-state model," *Smart Materials and Structures*, vol. 21, no. 5, p. 055009, 2012.

[26] U.S. Fish and Wildlife Service, "Feather atlas." `https://www.fws.gov/lab/featheratlas/`.

[27] R. R. Graham, "Safety devices in wings of birds," *Journal of the Royal Aeronautical Society*, vol. 36, no. 253, pp. 24–58, 1932.

[28] T. Alerstam, M. Rosén, J. Bäckman, P. G. Ericson, and O. Hellgren, "Flight speeds among bird species: allometric and phylogenetic effects," *PLoS Biol*, vol. 5, no. 8, p. e197, 2007.

[29] B. W. McCormick, *Aerodynamics, aeronautics, and flight mechanics*, vol. 2. Wiley New York, 1995.

[30] M. Niţă and D. Scholz, "Estimating the oswald factor from basic aircraft geometrical parameters," in *Deutsche Gesellschaft fr Luft- und Raumfahrt - Lilienthal-Oberth e.V., Bonn, 2012*, 2012.

[31] G. Sachs and M. A. Moelyadi, "Effect of slotted wing tips on yawing moment characteristics," *Journal of theoretical biology*, vol. 239, no. 1, pp. 93–100, 2006.

[32] P. Bourdin, A. Gatto, and M. Friswell, "Aircraft control via variable cant-angle winglets," *Journal of Aircraft*, vol. 45, no. 2, pp. 414–423, 2008.